Geophys. J. Int. (2001) **146,** 217–236

Electrical resistivity structure of the Valu Fa Ridge, Lau Basin, from marine controlled-source electromagnetic sounding

Lucy MacGregor,[1] Martin Sinha[1] and Steven Constable[2]

[1] *School of Ocean and Earth Science, Southampton Oceanography Centre, European Way, Southampton,* SO14 3ZH *UK. E-mail: lucym@soc.soton.ac.uk*

[2] *IGPP, Scripps Institution of Oceanography, La Jolla, California, USA*

Accepted 2001 February 16. Received 2001 February 16; in original form 2000 October 17

SUMMARY

In December 1995 we carried out a comprehensive controlled-source electromagnetic survey of the Valu Fa Ridge at 22°25′S in the Lau Basin. The Valu Fa Ridge is a back-arc spreading centre of intermediate spreading rate and is a site of extensive hydrothermal activity. Seismic studies have imaged a melt lens at an average depth of 3.2 km below the seafloor, surrounded by a zone of lowered seismic velocity, interpreted as a region of partial melt in the crust. The electromagnetic experiment was part of a multidisciplinary study which included wide-angle and reflection seismics, bathymetry and potential field measurements. Electromagnetic signals at frequencies between 0.25 and 40 Hz were transmitted from a horizontal electric dipole towed close to the seafloor and were recorded by an array of 11 sea-bottom receivers at ranges of up to 20 km from the source.

Over 80 hr of data, consisting of the magnitude of the horizontal electric field at the seafloor, were collected. These data have extremely low scatter compared to similar data from previous surveys. The data were interpreted using a combination of 1- and 2-D forward modelling and inversion. The vertical resistivity gradient in the upper crust at the Valu Fa Ridge is abnormally low, with resistivities of less than 10 Ω m observed throughout layer 2 of the crust to a depth of 3 km. This is significantly more conductive at depth than the axis of the slow-spreading Reykjanes Ridge at 57°45′N, and the fast-spreading East Pacific Rise at 13°N, where similar data sets have been collected in the past. Although the structure of layer 2 is well constrained by the electromagnetic data, its extremely low resistivity causes rapid attenuation of electromagnetic signals diffusing through it, and hence the data are not sensitive to the structure in layer 3, in particular the structure of the melt lens or surrounding low-velocity zone.

The seismic velocity structure of the Valu Fa Ridge, determined from the coincident wide-angle seismic study, is similar to that observed at other mid-ocean ridges, with a steep seismic velocity gradient through layer 2 (although overall velocities are slightly lower). The seismic velocity anomaly calculated relative to an average off-axis structure is also small. This suggests that the very low resistivities observed at the axis are not caused by an upper crust of abnormally high porosity. However, hot and/or saline fluids permeating the crust can explain the low resistivities without affecting the seismic velocity. Since the conductive region extends unbroken from 3 km depth to the seafloor, it is probable that these fluids circulate to (or close to) the magma chamber itself.

Key words: electrical resistivity, electromagnetic survey, mid-ocean ridge, Valu Fa Ridge.

INTRODUCTION

The complementary nature of electromagnetic and seismic measurements for the study of active spreading centres has been demonstrated in a variety of previous experiments (e.g. Sinha *et al.* 1998; Forsyth *et al.* 1998; Evans *et al.* 1999). Whilst the seismic method responds well to structural contrasts, electromagnetic methods are more sensitive to the bulk properties of a medium. Seismic velocity depends strongly on, among other things, porosity and crack geometry. In contrast, electrical resistivity is much more sensitive to the distribution of cracks, their interconnectedness and the properties of the pore fluids.

By collecting both data types, therefore, better constraints on the lithology and pore fluid properties can be obtained than from either technique alone. This in turn gives valuable information on the presence and properties of seawater or hydrothermal fluids in the upper crust and bodies of partial melt at deeper levels in the crust or upper mantle. In 1995 we carried out a multi-disciplinary study of the Valu Fa Ridge in the Lau Basin. The aim of the experiment was to collect coincident wide-angle seismic and controlled-source electromagnetic data from the ridge to give coincident determinations of velocity and electrical resistivity structure. In addition to the seismic and electromagnetic experiments, underway gravity, magnetic and bathymetry data were collected during the cruise. Results of the wide-angle seismic experiment have been presented by Turner *et al.* (1999). This paper reports the electromagnetic component of the study.

THE STUDY AREA

The Lau Basin is a small back-arc basin, separating the remnant Lau Ridge from the active Tofua Island Arc (Fig. 1). It is thought to have opened by the southward propagation of a spreading axis over the last 1–2 Myr. In the southeastern part of the Lau Basin this spreading axis is known as the Valu Fa Ridge (VFR) and lies 20–40 km west of the Tofua Island Arc. Spreading has been occurring at the Valu Fa Ridge for about the last 800 000 years, at a full rate of 60–70 mm yr^{-1} (Wiedicke & Collier 1993; Taylor *et al.* 1996). Previous swath bathymetry surveying (von Stackelberg *et al.* 1988) has shown that the VFR is divided into three morphological segments, the Northern, Central and Southern Valu Fa Ridges (NVFR, CVFR and SVFR respectively), which are separated by small overlapping spreading centres (OSCs). The survey described in this paper is located on the southern part of one of these segments, the CVFR.

The CVFR has been the target of a number of geophysical and geochemical studies. The impetus for these studies came from the discovery of a 2–3 km wide seismic reflector beneath the ridge, interpreted as the top of a magma chamber (Morton & Sleep 1985). This led to an extensive program of swath bathymetry surveying (von Stackelberg *et al.* 1988), bottom photography (von Stackelberg & Wiedicke 1990), dredging and geochemistry (Jenner *et al.* 1987; Herzig *et al.* 1990; Vallier *et al.* 1991), side-scan sonar surveying (Parson *et al.* 1990; Wiedicke & Kudrass 1990) and submersible dives (NAUTILAU group 1990; Fouquet *et al.* 1991a,b). The high volatile content of the erupted magma produces extremely vesicular volcanics, which degenerate quickly at the seafloor into loose fragments with little cohesion. The unconsolidated volcanic fragments allow extensive circulation of seawater and hydrothermal fluids, giving rise to abundant and widespread seafloor and subsurface mineralization. In many areas manganese- and iron-rich crusts (some up to 10 cm thick) have been observed at the seafloor, produced by extensive low-temperature discharge related to the high permeability of the seafloor (von Stackelberg *et al.* 1988; Fouquet *et al.* 1991b). There is also active high-temperature hydrothermal activity. The Vai Lili hydrothermal field, situated at the northern end of the CVFR, produces hydrothermal fluids at temperatures of up to 400 °C (NAUTILAU group 1990; Fouquet *et al.* 1991a,b)

In 1988 the CVFR was the target of a large seismic reflection experiment, presented by Collier & Sinha (1992a,b). The experiment covered an area of 30 by 45 km, between the overlap of the CVFR and NVFR at 22°10′S, and the onset of the overlap between the CVFR and the SVFR at 22°27′S. Throughout this survey area a bright, reversed-polarity reflector was seen on the seismic data at 4.2–4.3 s two-way-time. This was interpreted as the roof of a crustal magma chamber at a depth of, on average, 3.2 km below the seafloor, which appeared to be an unbroken feature throughout the survey area. The width of the magma chamber varied between 0.6 and 2.3 km beneath most of the CVFR, widening to around 4 km beneath the OSC at 22°10′S. Results of the 1995 wide-angle survey (Turner *et al.* 1999) show that the melt lens imaged by the reflection experiment is surrounded by a small low-velocity zone, in which seismic velocities are depressed by up to 0.4 km s^{-1} relative to the average velocity in layer 3. This is consistent with a region containing a very low melt fraction ($\sim$1 per cent) extending beneath the magma chamber to within 2–3 km of the Moho.

The CVFR itself can be subdivided into volcanic segments (Wiedicke & Collier 1993), characterized by undulations in the seafloor of length 6–12 km and amplitude 100–300 m. The segmentation is also reflected in the morphology of the ridge and the properties and geometry of the magma chamber reflector. This observation led to the conclusion that each section of the CVFR has a different volcanic history, driven by variations in melt supply both along strike and with time (Collier & Sinha 1992b; Wiedicke & Collier 1993). Similar cycles of magmatic activity punctuating longer periods of amagmatic extension and faulting have been observed at other spreading centres (Parson *et al.* 1993; Sinha *et al.* 1998). The northern section of the CVFR is bathymetrically the shallowest, with no evidence of tectonic faulting, and is characterized by fresh volcanics. The width of the melt lens is greatest beneath the overlap between the CVFR and NVFR. These observations suggest that the northern part of the CVFR is currently a site of active volcanism. The central section of the CVFR is slightly deeper with some faulting on the western flank. The melt lens is narrow beneath this section of the ridge (0.6–1.0 km). The southern section of the CVFR is heavily faulted and degraded, with highly weathered volcanics and little evidence of recent volcanism. However, the melt lens under this section of the CVFR is wide (1.5–2.3 km), and is characterized by an extremely bright seismic reflection. This suggests that although this section of the ridge is volcanically inactive at present, the wide melt lens may be the result of a recent influx of melt, signalling the onset of a new magmatic phase (Collier & Sinha 1992b). The electromagnetic experiment described here was centred on this southern section of the CVFR (Fig. 1).

THE METHOD

For this study we used controlled-source electromagnetic (CSEM) sounding in the frequency domain (e.g. Young & Cox 1981; Sinha *et al.* 1990). The CSEM method uses a horizontal electric dipole source to transmit a discrete frequency electromagnetic signal to an array of sea-bottom receivers which detect and record the horizontal electric field at the seafloor. During the survey the source is towed within an array of seafloor receiving instruments. By studying the variation in the amplitude and phase of the received electric field as a function of source–receiver separation and geometry, and the frequency of the signal, the resistivity structure of the underlying crust can be determined. Frequencies between a few tenths and a few tens

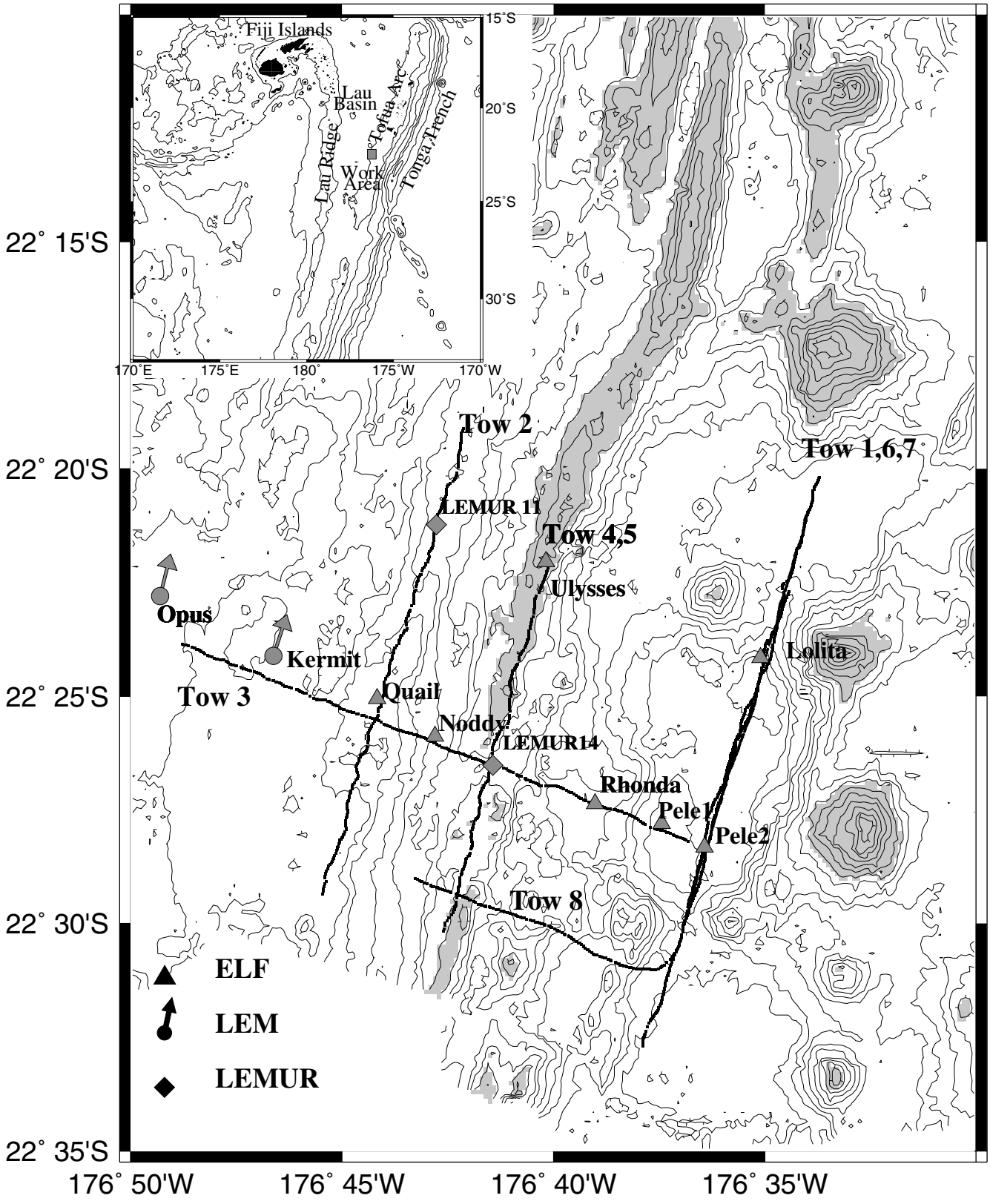

Figure 1. Bathymetry of the Central Valu Fa Ridge (CVFR) and the experimental configuration. The contour interval is 100 m and seafloor shallower than 2000 m has been shaded to show the position of the ridge axis. Electric field receiver locations are shown along with the positions of the source tow tracks. The arrows on the LEM instruments show the direction of their 300 m receiver dipoles. Tow 3 is coincident with the southern wide-angle seismic line of Turner *et al.* (1999). The inset shows the position of the work area in the Lau Basin.

of Hertz are transmitted in a typical survey. Although transmission at several different frequencies across this band is desirable since it allows resolution of structure on several length scales, both the vertical and horizontal resolutions of the technique come primarily from geometric effects. Depths of investigation up to 30 km have been achieved in the past over mature oceanic lithosphere (Constable & Cox 1996), although at ridges, where the resistivity of the crustal rocks is lower, the CSEM technique is most effective for probing shallower (0–5 km depth) structure (e.g. Evans *et al.* 1994; MacGregor *et al.* 1998).

THE EXPERIMENT

The source, Cambridge University's DASI (deep-towed active source instrument, now based at the Southampton Oceanography Centre), consists of a neutrally buoyant, 100 m long horizontal electric dipole (HED), streamed behind a deep-towed vehicle (Sinha *et al.* 1990). This was towed above the sea-bottom at heights less than a skin depth in seawater (where the skin depth is the distance over which the amplitude of the field decays by a factor of e) to ensure good coupling of electromagnetic energy onto the crust. The height of the source above the seafloor was monitored acoustically using a 3.5 kHz echo-sounder mounted on the deep-tow vehicle. The source transmitted a pseudo-square waveform with an amplitude of typically 300 A peak-to-peak, to give a source dipole moment of about 10^4 A m. Four ancillary electrodes spaced along the main source dipole and connected to a logger (the DASI logger) on the deep-tow allowed independent monitoring of the transmitted fields. The source position was determined by acoustic ranging between the ship, the deep-tow and the seafloor instruments augmented by an array of navigation transponders.

Three types of receiver were deployed. The Scripps ELFs (electric field instruments) and Cambridge LEMURs (low-frequency electromagnetic underwater receivers, also now based in Southampton) record two orthogonal components of the horizontal electric field at the seafloor using a pair of 10 m long HED receivers (Sinha *et al.* 1990; Constable & Cox 1996). These receivers can detect source signals out to distances of around 10–15 km from the source. The Scripps LEM (long-wire electromagnetic) instruments have a single long antenna (300 m in this experiment) which is streamed on the seafloor behind the LEM instrument package (Webb *et al.* 1985; Constable & Cox 1996). Although the LEM instruments detect only one component of the seafloor electric field, the long receiver dipole makes them more sensitive than the short-arm ELFs and LEMURs, allowing signals at source–receiver separations of 20–30 km to be detected.

The geometry of the CSEM survey is illustrated in Fig. 1. Data were retrieved from nine ELF/LEMUR instruments and two LEM instruments, which were deployed in an array along and across the ridge axis. The instrument array and the tow locations were designed to maximize the range of source–receiver geometries in the data set, and hence maximize the sensitivity of the survey to both 1-D and 2-D structure beneath the ridge axis (Unsworth 1991; MacGregor *et al.* 1998, MacGregor & Sinha 2000). The source was towed along five tracks, along and across the ridge axis, to give a total of 80 hr of data at fundamental transmission frequencies of 0.25, 1 and 8 Hz. The across-axis tow 3 was coincident with the southern wide-angle seismic line (Turner *et al.* 1999) collected as part of the study. The electromagnetic data are summarized in Table 1 and cover source–receiver separations of 500 m to 20 km.

DATA REDUCTION

The raw data are continuous, unstacked time-series collected at sampling rates of 128 and 64 Hz on the LEMUR and ELF/LEM instruments respectively. Initial data reduction consisted of dividing the recorded time-series up into 256 s segments and applying a fast Fourier transform (FFT) to each to extract the amplitude and phase of the signal at the fundamental transmission frequency and its third and fifth harmonics (the amplitudes of the second and fourth harmonics are small since the source transmits a pseudo-square wave). An example of the raw time-series data recorded by a short-arm instrument when the transmission frequency was 1 Hz is shown in Fig. 2(a).

Table 1. Summary of the data collected. In all, 80 hrs of data were collected along 134 km of source tow line. The source dipole moment was calculated from the DASI logger data and calibrations during pre- and post-deployment deck tests. The final column of the table lists the instruments from which data for each tow were retrieved. The first letter of the instrument name is given in the case of the ELFs, and the LEMURs are identified by their numbers. Instrument *Pele* was recovered at the end of tow 1 and re-deployed for the remainder of the experiment. The two deployments are labelled p1 and p2 respectively. Tows 1, 6 and 7 followed the same tow track, at three different transmission frequencies. Tow 4 was aborted after 2 km due to source malfunction, and restarted as tow 5. Source instabilities during tow 7 severely degraded the quality of the data, hence they were not included in the analysis.

Tow	Frequency (Hz)	Dipole moment (A m)	Length (km)	Duration (hr)	Instruments
1	1.0	12 000	21	11	p1,r
2	1.0	12 000	20	11	L11,n,L14,r,k,o
3	8.0	12 000	23	18	p2,r,L14,n,k,o
4	1.0	12 000	2	2	u
5	1.0	12 000	16	10	L11,u,q,n,p2,k,o
6	0.25	4500	19	11	p2,l,n,k
7	8.0	4500	21	11	l,p2
8	1.0/0.25	4500	12	6	p2

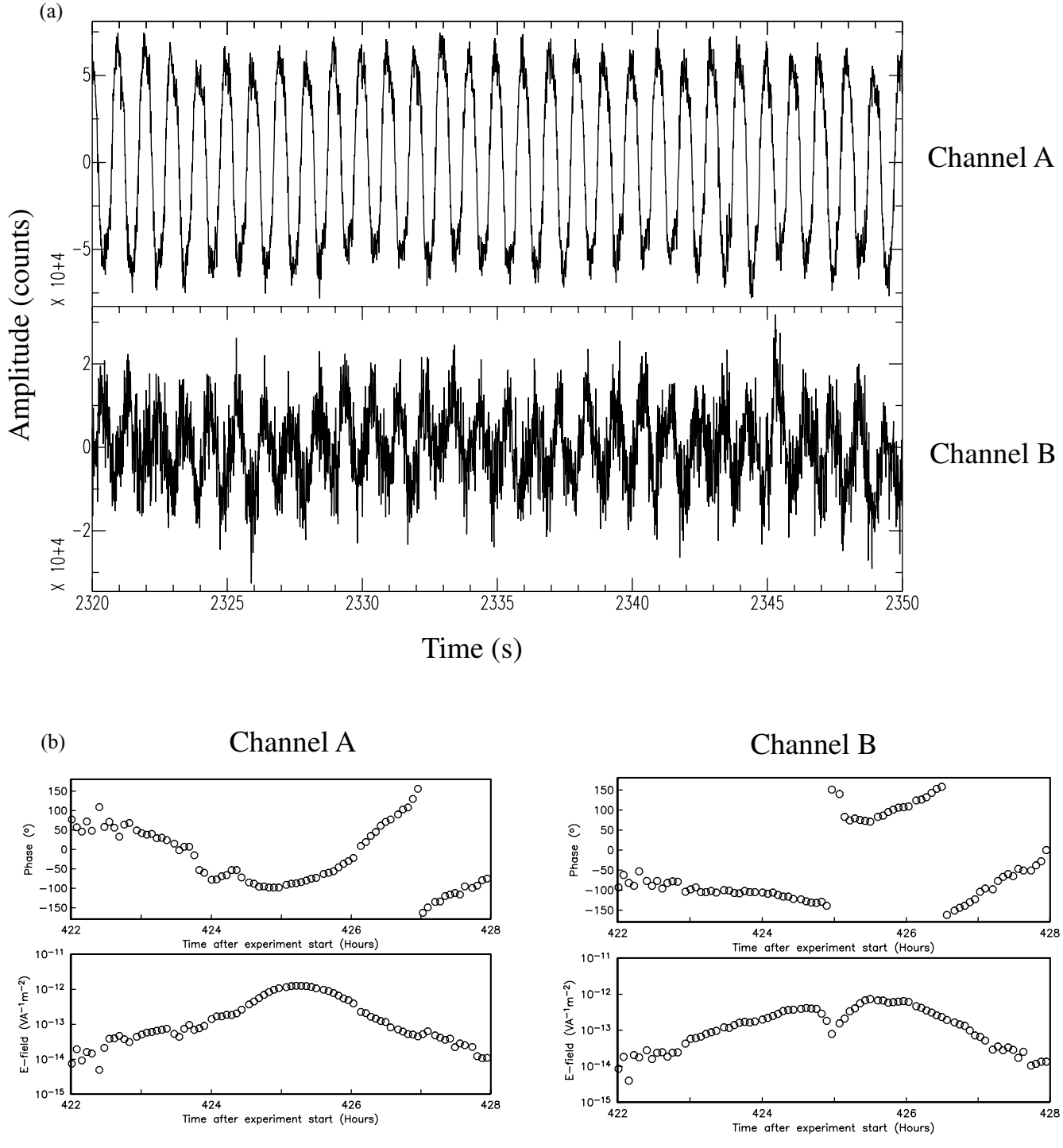

Figure 2. (a) Raw time-series recorded during tow 2 on the two orthogonal channels of a short-arm instrument. The transmission frequency was 1 Hz. (b) Amplitude and phase of the signal at 1 Hz as a function of time during tow 5 recorded by *Noddy*. Each point is derived from an FFT of a 256 s long segment of the raw time-series. Amplitudes have been normalized by the source dipole moment during the tow and corrected for the frequency response of the instrument. The phase data have been corrected for the drift in the source phase during the experiment. Channel A was oriented along 178°, almost parallel to the source, and therefore the amplitude is maximum on this channel at the closest point of approach of the source. The orthogonal channel displays a corresponding minimum at the closest point of approach. Both the amplitude and phase data have a very low scatter.

Fig. 2(b) shows the amplitude and phase of the 1 Hz component of the signal from *Noddy* as a function of time during tow 5. Both the amplitude and phase of the signal have extremely low scatter, in contrast to data collected in previous CSEM surveys at mid-ocean ridge crests (Evans *et al.* 1991, 1994; MacGregor *et al.* 1998). In previous surveys the high degree of scatter was attributed to near-surface heterogeneity. The lack of scatter in the current study, especially at lower

frequencies, suggests that either the shallow structure at the Valu Fa Ridge lacks the heterogeneity observed at the East Pacific Rise or Reykjanes Ridge, or much of the scatter in the earlier experiments was due to instabilities in the source.

Data at the longest ranges were corrected for drift in the source phase (determined using data from the DASI logger) and then stacked over longer time windows to improve signal-to-noise ratio, and hence extend the range to which source transmissions could be detected. The largest stack-fold was 84 (corresponding to a 6 hr stack of data for the 0.25 Hz LEM data from tow 6, for which the source–receiver range and geometry varied slowly during the tow). All amplitudes were then corrected for the height of the transmitter above the seafloor assuming exponential decay of the fields in the seawater, corrected to take account of the frequency response of the receivers and finally normalized by the source dipole moment to allow easy comparison with modelling results.

The LEM instruments only record a single component of the seafloor electric field and so these amplitudes form the basis of modelling and interpretation. The data recorded by the two orthogonal channels of the ELF/LEMUR instruments can be further decomposed to yield polarization ellipse parameters (Smith & Ward 1974). The semi-major axis of the polarization ellipse is a more robust measure of the seafloor electric field than either of the two components separately (Constable & Cox 1996; MacGregor *et al.* 1998). The orientation of the polarization ellipse depends strongly on the orientations of the source and receiver, both of which are subject to error, and was therefore excluded from the analysis. Although this results in some loss of information, synthetic modelling studies show that the semi-major axis of the polarization ellipse can be used to recover the bulk resistivity of a medium and in particular can constrain both horizontal and vertical resistivity gradients.

Ambient noise levels were estimated by applying the same FFT procedure to time-series recorded prior to the start of transmission, and during the 16 hr break in transmission between tows 3 and 4. To a good approximation the noise may be assumed to be Gaussian, and the standard deviations of the real and imaginary components from the FFT combined to give a single parameter characterizing the noise level (Constable & Cox 1996). These noise parameters are shown in Fig. 3, normalized by a source dipole moment of 12 000 A m to allow direct comparison with the data. External noise sources include electromagnetic fields from ionospheric and cultural sources and motionally induced fields caused by water currents, microseisms and earthquakes (Webb & Cox 1982, 1986). Internal noise is generated in the electrodes and the instrument electronics. The majority of instruments exhibit a red noise spectrum, caused by a combination of electrode noise and ionospheric noise beginning to leak through the conductive ocean layer at low frequencies.

The noise values were used to obtain an estimate of the error on the data amplitudes. As long as the signal-to-noise ratio is large enough and the component distributions have equal variance, the standard deviations of the real and imaginary components of the noise data can be used as normally distributed errors on the data (Constable & Cox 1996). The errors calculated in this way have a range-dependent variation as expected, being less than 1 per cent when the source is close to instrument and signal levels are greatest, rising to 20 per cent at

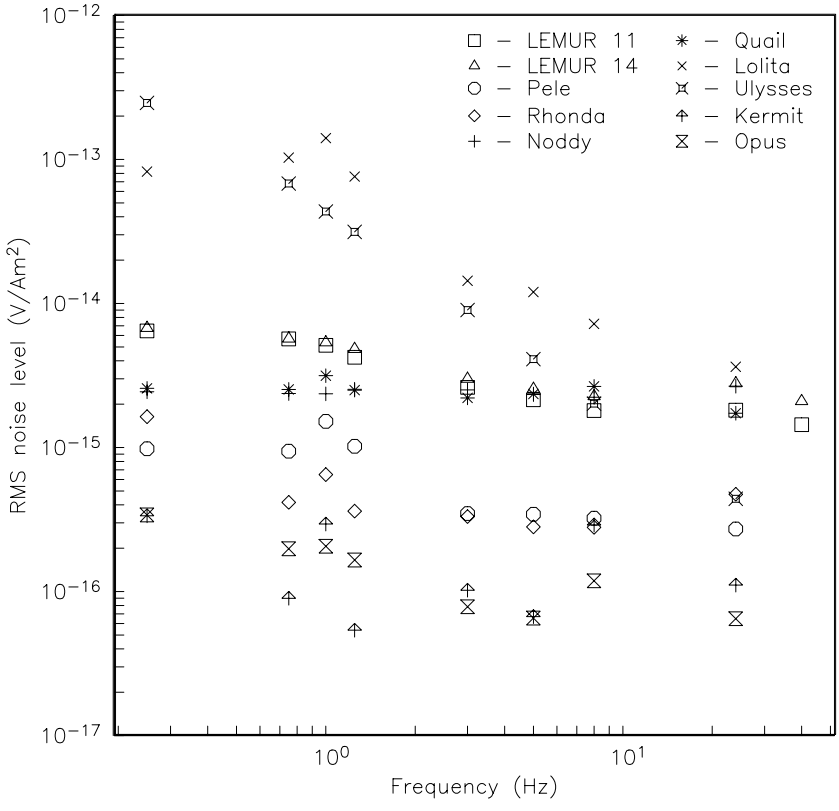

Figure 3. Noise levels on the ELF and LEM instruments, defined as the RMS electric field in a bandwidth of 0.004 Hz. Frequencies are chosen to cover the range transmitted during the experiment. Values have been normalized by 12 000 A m, the source dipole moment, to allow direct comparison with the data.

a distance of about 8, 6 and 3 km from the source for the 0.25, 1 and 8 Hz data respectively (the percentage error rises faster for the higher frequency data because the magnitude of the field falls off faster with distance).

The errors calculated on the basis of noise estimates alone take no account of scatter in the data caused by the motion of the source over small-scale heterogeneities in the upper crust, nor of uncertainties in the experimental geometry. Much of the scatter in previous CSEM data sets was attributed to surface heterogeneity (Evans *et al.* 1991, 1994; MacGregor *et al.* 1998). Unsworth (1994) predicted on the basis of modelling that the motion of the source over 100 m scale surface inhomogeneities with a factor of five variation in conductivity would result in a range-independent scatter of 3 per cent at 1 Hz, rising to 8 per cent at 8 Hz (at higher frequency the scale of the inhomogeneities is a larger fraction of a skin depth, so their effect on the measured signal is greater). The largest contribution to geometric errors is the effect of uncertainty in the source–receiver separation, which increases as a proportion as the source approaches the receiver. The magnitude of the effect also depends on the frequency of the transmitted field and the resistivity of the seafloor, because the shift in the electric field increases as the error in separation becomes a greater fraction of the skin depth. On the basis of acoustic positioning of the source and receivers during the survey, the error in source–receiver separation is estimated to be about 100 m. Table 2 shows the percentage change in the electric field caused by a 100 m change in separation, for the range of frequencies spanning that in the data. At short ranges, the effect of uncertainties in source–receiver geometry dominates. At longer ranges errors calculated on the basis of noise estimates dominate. On the basis of the values in Table 2, minimum data errors were set to 15 per cent for the 0.25 and 1 Hz data, 30 per cent for the 8 Hz data and 50 per cent for the 24 Hz data.

MODELLING THE DATA IN ONE DIMENSION: SHALLOW STRUCTURE

Until recently the main method of interpreting marine CSEM data of the type collected has been regularized inversion in terms of 1-D resistivity structures using the forward code of Chave & Cox (1982) and the Occam inversion algorithm of Constable *et al.* (1987), implemented for seafloor CSEM data by Flosadóttir & Constable (1996). Although in a mid-ocean ridge environment it is unlikely that the resistivity structure is in reality 1-D, the assumption of one-dimensionality provides a simple starting point. This assumption is particularly applicable to the data from tow 3, which runs perpendicular to the ridge axis (Fig. 1). The transmission frequency was 8 Hz during this tow. Because the electromagnetic skin depth is shortest at high frequency, these data are most sensitive to the shallow structure local to each instrument and are less affected by larger-scale along- and across-axis variations in resistivity. The data quality is high, so data at both the fundamental transmission frequency and its third harmonic (24 Hz) were used. The tow 3 data set is shown in Fig. 4 and consists of electric field strength as a function of source–receiver separation for the two LEM instruments (*Kermit* and *Opus*), and four ELF/LEMUR instruments (*Noddy*, *LEMUR14*, *Rhone* and *Pele2*), which are placed between 15 km west of the ridge axis and 9 km east.

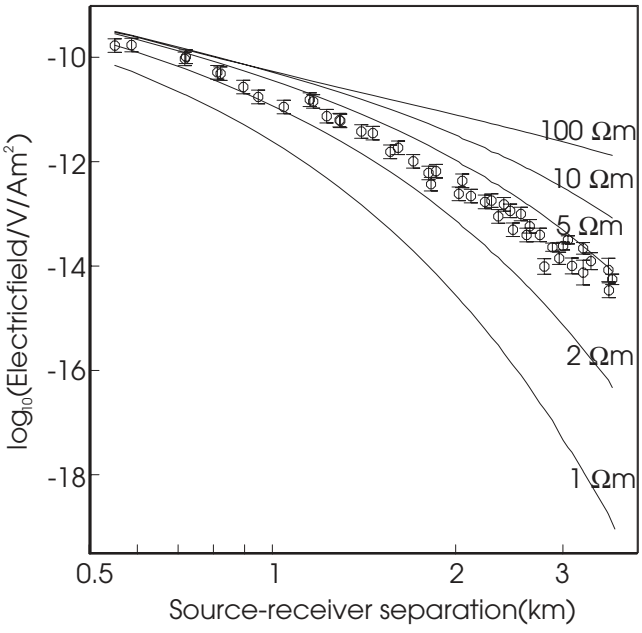

Figure 4. The effect of seafloor resistivity on electric field strength. Circles show the 8 Hz data from *LEMUR14* collected during tow 3. Overlain are the responses of five double half-space models in which the upper half-spaces (with resistivity 0.3 Ω m) represents the ocean, and the lower half-spaces represent the crust and have resistivities of 1, 2, 5, 10 and 100 Ω m. The data cannot be explained by a single half-space model; however, they parallel the half-space responses closely, suggesting that the vertical resistivity gradient in the upper crust at the CVFR is low.

Table 2. The percentage shift in the electric field at distances of 1, 2 and 5 km along the dipole axis, for a change in the source–receiver separation of 100 m. The effect of an uncertainty in the separation of the source and receiver is largest at small separations and also depends on the frequency of the signal and the resistivity of the seafloor. Values were calculated for three seafloor resistivities, similar to those encountered in the Lau Basin, over the range of frequencies transmitted during the survey.

Frequency	2 Ω m			5 Ω m			10 Ω m		
	1 km	2 km	5 km	1 km	2 km	5 km	1 km	2 km	5 km
0.25 Hz	30%	15%	10%	30%	12%	7%	31%	11%	6%
1 Hz	26%	19%	16%	20%	15%	11%	21%	14%	9%
8 Hz	42%	38%	37%	30%	27%	25%	27%	22%	19%
24 Hz	56%	53%	53%	43%	40%	43%	35%	31%	29%

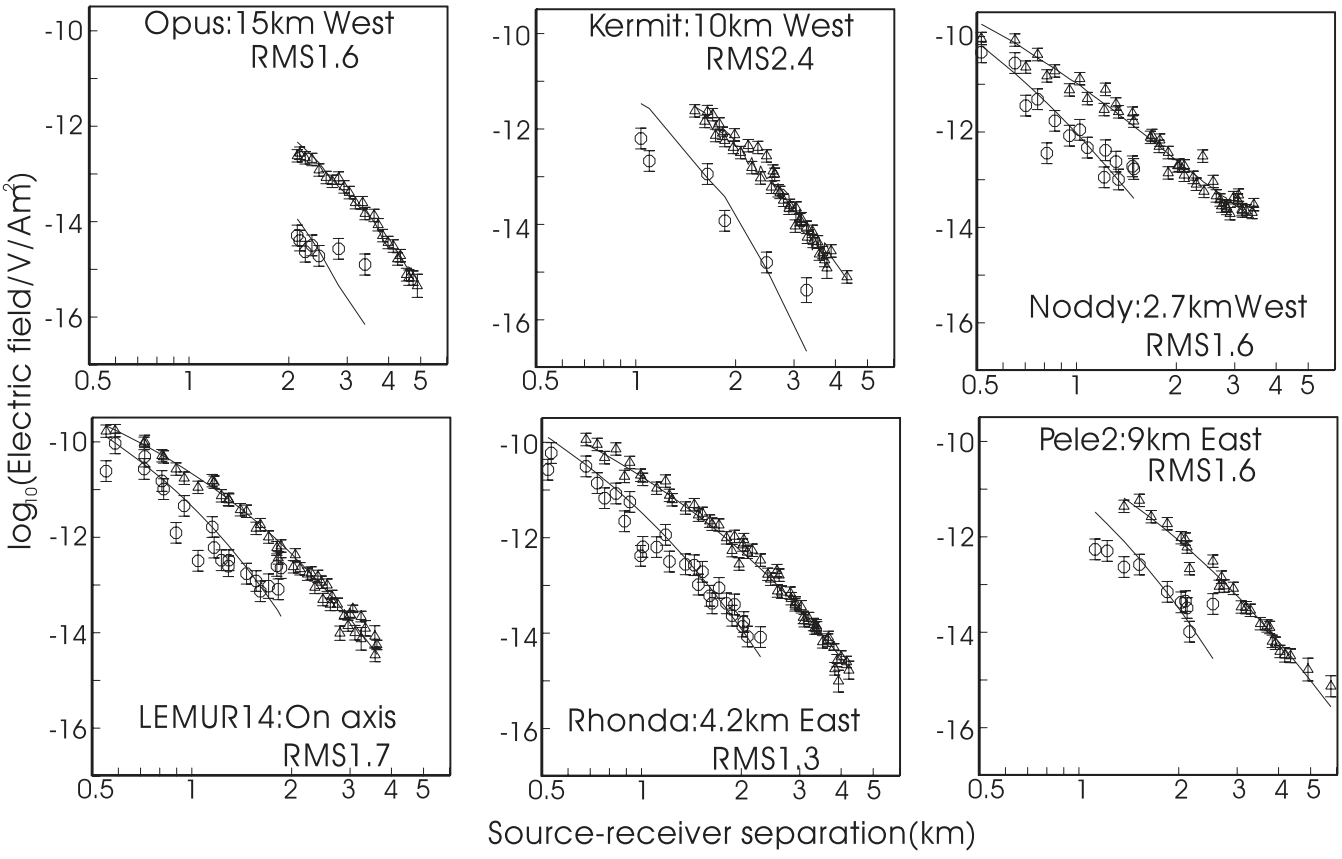

Figure 5. Data collected during tow 3, consisting of electric field strength as a function of source–receiver separation at the 8 Hz transmission frequency (triangles) and its third harmonic, 24 Hz (circles). Error bars show one standard deviation, calculated from the noise distribution, with minimum values of 30 and 50 per cent for the 8 and 24 Hz data respectively. The position of each instrument relative to the ridge crest is given. The responses of the 1-D models plotted in Fig. 6 are shown along with the RMS misfit of each.

Before proceeding, it is useful to illustrate the effect of seafloor resistivity on the data. Fig. 5 shows the 8 Hz data from *LEMUR14* (located on the ridge axis). Overlain on this are the responses of five different uniform half-space models. For a given frequency, the lower the resistivity of the seafloor, the faster the rate of decay of the electric field strength with distance from the source. The depth to which data are sensitive increases with increasing source–receiver separation. Fig. 5 shows that whilst the shortest range data agree most closely with the 2 Ω m curve, the longer-range data are close to the 5 Ω m curve, indicating that there is an increase in resistivity with depth below the seafloor. However, the data parallel the half-space response curves remarkably closely. From this we can infer that the vertical resistivity gradient is low, a result which is borne out by the modelling results.

The 8 and 24 Hz data from each receiver were inverted jointly using the Occam algorithm to minimize the second derivative of resistivity with respect to depth to produce models as closely resembling a linear resistivity gradient with depth as allowed by the data. The corresponding models are shown in Fig. 6. The data constrain the resistivity structure to a depth of about 1 km below the seafloor. This corresponds to the upper part of the seismically defined layer 2A, which has an average thickness of 1.3 km at the Valu Fa Ridge (Turner *et al.* 1999).

The results indicate a remarkable uniformity in the structure of layer 2A between 15 km west of the axis and 9 km east. In all cases the resistivity rises from 1–3 Ω m at the seafloor, to

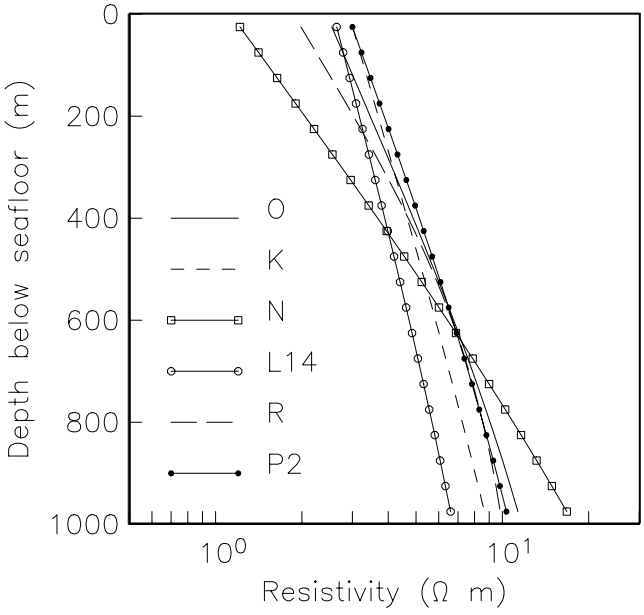

Figure 6. Models resulting from the joint inversion of the 8 and 24 Hz data shown in Fig. 4. The inversion minimized the second derivative of resistivity with respect to depth to produce models as close to a linear resistivity gradient with depth as was compatible with the data. All models are overlain by a uniform half-space of resistivity 0.3 Ω m representing the ocean.

6–10 Ω m at a depth of 800 m. Geochemical data from DSDP drilling suggest that alteration within the upper oceanic continues for about 13 Myr after crustal formation, and may last as long as 20 Myr (Staudigel *et al.* 1986). The oldest crust sampled in this study is 0.5 Myr (located at instrument *Opus*, 15 km west of the axis). All the instruments are therefore located on relatively 'young' crust, so the lack of variation in the resistivity structure of layer 2A is unsurprising. The one outlier is the result from instrument *Noddy*, which exhibits a significantly lower resistivity in the upper 200–300 m of the structure. Instrument *Noddy* is located at the bottom of a slope on the western flank of the ridge axis and might therefore be located on a pile of loose fragments or scree slope, which is a possible explanation for the low resistivity local to the instrument. There is some indication that the structure beneath *LEMUR14*, located on the ridge axis may be slightly more conductive at a depth of 800 m than at the other sites, but the difference is not large.

These results contrast strongly with the results of previous CSEM experiments on mid-ocean ridge axes. Similar experiments have been performed at the East Pacific Rise (EPR) at 13°N (Evans *et al.* 1991 1994), where the full spreading rate is 100 mm yr^{-1}, and at the Reykjanes Ridge at 57°45′N (MacGregor *et al.* 1998), where the full spreading rate is 20 mm yr^{-1}. Although the resistivity close to the seafloor at these sites is similar to that observed at the VFR, in both cases the vertical resistivity gradient in the upper crust is significantly steeper, with the result that at 800 m below the seafloor, the resistivity is about 40 Ω m at the Reykjanes Ridge and about 80 Ω m at the EPR, almost an order of magnitude more resistive than the VFR. There is clearly no simple relationship between upper crustal resistivity and spreading rate. The difference is likely to be related to the high volatile content and high viscosity of the magma produced at the Valu Fa Ridge (as compared to the basalts of normal mid-ocean ridges), which produces a large volume of extrusives in which porosity and permeability decrease much more slowly with depth than at other ridges.

MODELLING THE DATA IN TWO DIMENSIONS

To look at larger-scale, deeper structure, the remaining 1 and 0.25 Hz data at longer source–receiver separations must be examined, and for these data the assumption of one-dimensionality is clearly invalid. Although a code for modelling this type of data in terms of full 3-D resistivity structures is under development (Flosadóttir & MacGregor 1999), it cannot as yet be applied to real data. The data are therefore interpreted in the remainder of this paper using a combination of 2.5-D forward modelling and inversion.

The response of a 2-D resistivity structure to the 3-D fields of a point horizontal electric dipole (known as a 2.5-D problem) is calculated using the finite element code of Unsworth *et al.* (1993). In order to overcome numerical problems associated with the singularity at the source, the electromagnetic fields are separated into a primary component, calculated analytically for a simple double half-space model, and a secondary component. The secondary fields are calculated for the difference between the total 2-D structure of interest and the 1-D background structure using the finite element method. In order to model the exponential decay of the fields accurately, at least three elements per skin depth are required (Unsworth 1991). The number of elements required in a finite element mesh to obtain an accurate solution increases rapidly with increasing frequency because of this.

Although an inversion of CSEM data of this type based on a subspace approach has been developed by Unsworth & Oldenburg (1995), their code cannot model the complicated source–receiver geometries encountered in a real experiment. The inversion used here is based on the Occam algorithm (Constable *et al.* 1987; de Groot–Hedlin & Constable 1990), implemented for the CSEM case by MacGregor (1999) to allow realistic experimental geometries to be incorporated. The Occam approach has a number of advantages. The inversion is completely general, requiring no *a priori* knowledge of the resistivity structure. However, if such information exists it can be easily incorporated to add extra constraints to the inversion.

Along-axis variability

Modelling would be significantly simpler if it could be assumed that the structure of the CVFR is invariant parallel to the strike of the ridge. This would allow an interpretation solely in terms of vertical and across-axis variations (variations in structure with depth and with age of the crust). There are, however, features in the data which indicate that the structure varies along-axis as well. These are illustrated in Fig. 7(a), which shows the 1 Hz data from *LEMUR11* and *Noddy* plotted as a function of position along tow 2. There is a marked asymmetry in the data about the instrument locations. For both receivers, data collected when the source was north of the receiver have a lower magnitude than data collected when the source was to the south. Since for any given source–receiver separation, the geometry and transmission characteristics are the same regardless of the location of the source, this difference indicates a variation in the structure along the strike of the ridge. A similar (although less pronounced) variation is seen in the data collected by *Ulysses* and *Noddy* during tow 5 (also 1 Hz transmission) shown in Fig. 8.

To examine this variation further, the data from *LEMUR11* and *Noddy* shown in Fig. 7(a) were inverted for a 2-D resistivity structure parallel to the ridge axis (the resistivity was assumed to be invariant perpendicular to the axis of the ridge). The data used were limited to the 1 Hz, tow 2 data from these instruments to minimize the effect of across-axis variations in structure with respect to along-axis variations. The forward computation requires primary fields, calculated analytically for a simple double half-space model at each node in the finite element mesh, for each source position specified (Unsworth *et al.* 1993). Since the sensitivity calculation, which uses the adjoint method of McGillivray *et al.* (1994), requires the electromagnetic fields from a source placed at each source and receiver location, the memory requirements increase rapidly with the number of both sources and receivers specified in the inversion. To make the problem computationally tractable, the data shown in Fig. 7(a) were partitioned into along-track bins at 1 km spacings, thus reducing to 21 the number of different source locations required to describe the data set. In order to keep the forward solution stable, the difference in resistivity between the primary double half-space model and the 2-D structure of interest must be small close to the source. To ensure that this was the case during the inversion, the upper 400 m of the model

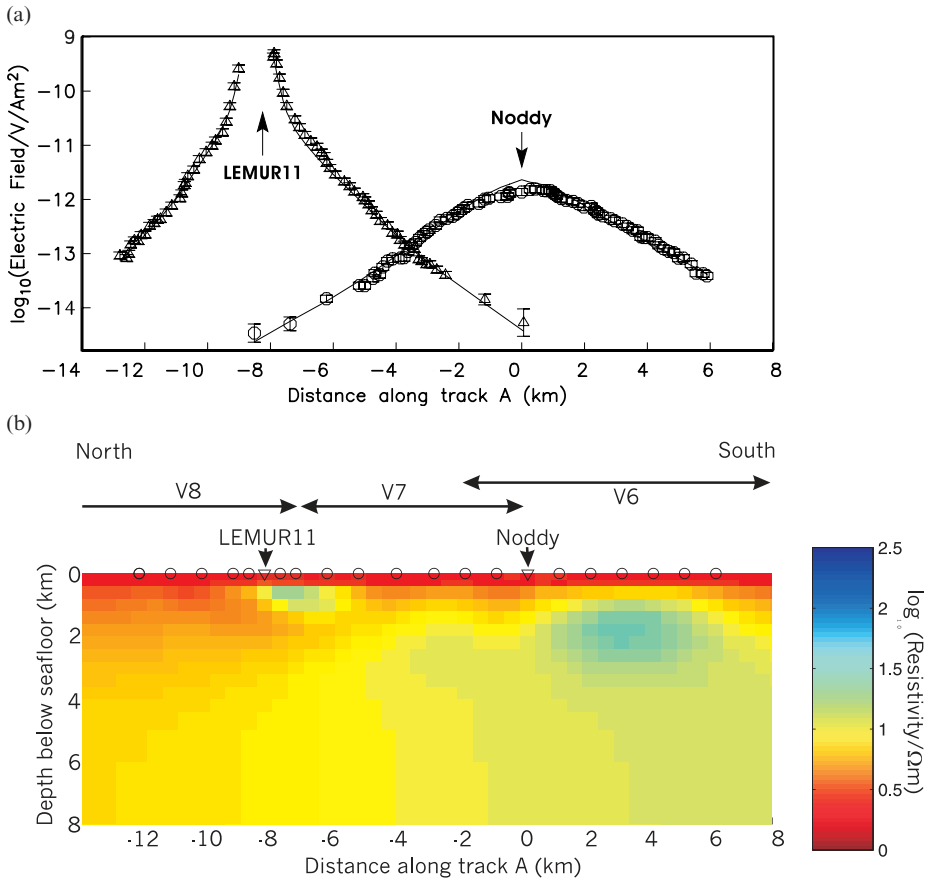

Figure 7. (a) Data at 1 Hz from *LEMUR11* and *Noddy* collected during tow 2, plotted as a function of distance along tow 2 from its intersection with tow 3. *LEMUR11* lies on tow 2 whilst *Noddy* is 2.7 km off the tow line itself. There is a marked asymmetry in the data about the instrument locations, which indicates that the structure of the ridge varies along strike. The solid line shows the response of the model shown in (b), which fits the complete (unbinned) data set to RMS 1.3. (b) Model resulting from inversion of binned data derived from that shown in (a), plotted without vertical exaggeration. The model is overlain by a uniform half-space of 0.3 Ω m representing the ocean, and is invariant perpendicular to the plane of the page. The model shows a vertical resistivity section parallel to the strike of the ridge, and centred approximately 3.8 km west of the axis. Instrument positions are shown by triangles at the seafloor. The circles show the source positions used in the inversion. There is a general increase in resistivity to the south (right-hand end of the figure). Also shown are the extents of fourth-order segments V6, V7 and V8, as defined by Wiedicke & Collier (1993) in terms of seafloor morphology and magma chamber properties.

were prejudiced to tend to 2 Ω m, the primary resistivity chosen on the basis of the 1-D inversions of the tow 3 data. This was sufficient to ensure the stability of the forward solution, without having to fix any of the model parameters (and hence unduly influence the inversion).

The model resulting from the inversion is shown in Fig. 7(b). The inversion started from a 400 m thick layer of resistivity 2 Ω m, overlying a 10 Ω m half-space. The response of the model fits the entire data set shown in Fig. 7(a) to an RMS misfit of 1.3. The remaining bias in the residuals is likely to be due to 3-D effects in the data. The model represents a vertical resistivity section parallel to the ridge and centred about 3.8 km west of the axis (midway between tow 2 and instrument *Noddy*). The data constrain the structure to a depth of about 3 km, between −12 km and 7 km along track. Outside this area the structure is controlled by the requirement in the inversion that the model be smooth. The model shows a steady increase in resistivity to the south (right-hand end of the figure), required to explain the steady increase in data amplitudes to the south for a given source–receiver separation and geometry.

Fig. 8 shows the equivalent result for 1 Hz data from *Noddy* and *Ulysses* collected during tow 5 (along the ridge axis). The model again represents a vertical resistivity section parallel to the ridge, but in this case much closer to it (about 1.25 km away from the axis). The along-axis extent of the data from tow 5 shown in Fig. 8 is smaller than that of the tow 2 data, with the result that the data constrain the model between along-track distances of −8 and 6 km. Despite this, the structure is significantly different from that in Fig. 7, showing that the overall resistivity structure is 3-D in nature. In addition to being much more conductive, the variation in the structure along the ridge axis is much less pronounced than that 3.8 km to the west.

Also shown in Figs 7 and 8 are the fourth-order volcanic segments of the ridge, defined by Wiedicke & Collier (1993). Segment V7 is underlain by a 1.5–2.3 km wide magma chamber reflector of high reflection coefficient. Although this segment of the ridge is heavily faulted and weathered with little evidence of recent volcanic activity, Collier & Sinha (1992b) suggest that the wide, bright magma chamber may be a consequence of a recent influx of melt signalling the start of a new magmatic

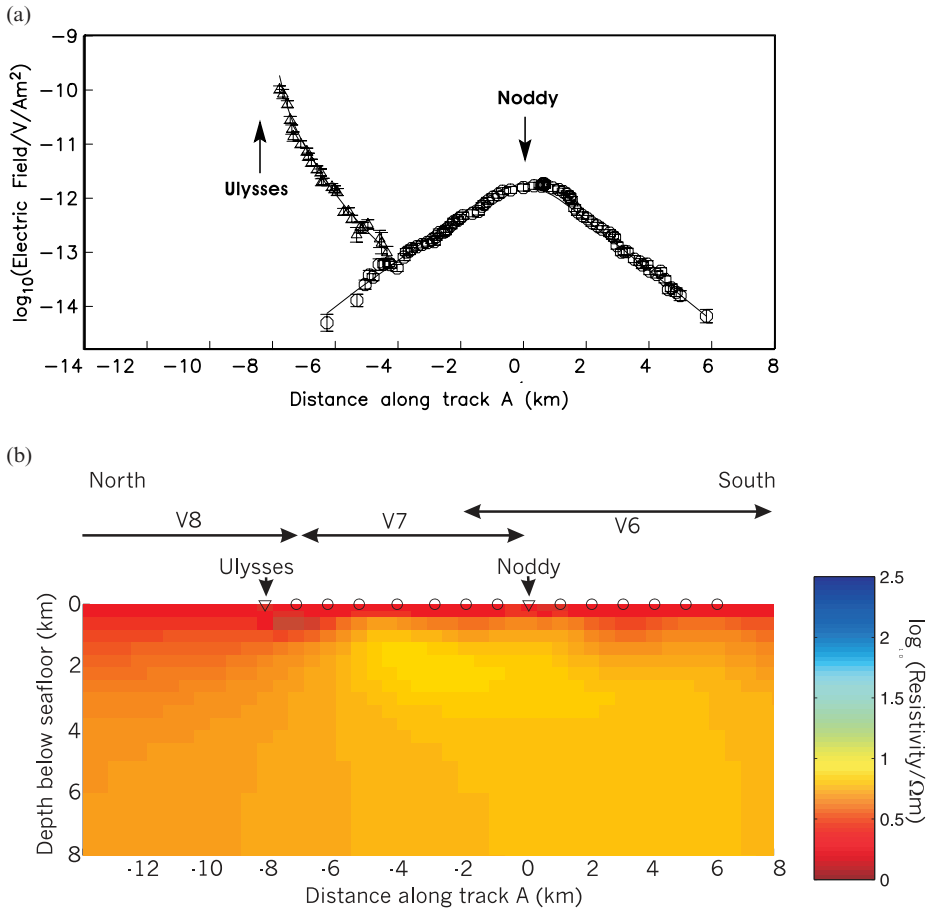

Figure 8. (a) Data at 1 Hz from *Ulysses* and *Noddy* collected during tow 5, plotted as a function of distance along tow 5 from its intersection with tow 3. *Ulysses* lies on the tow line, whereas *Noddy* lies 2.7 km to the west of the tow. The asymmetry in the data about the instrument location is much less marked for the along-axis tow 5 than for tow 2, which was 5 km west of the axis. The solid line shows the response of the model shown in (b), which fits the data to RMS 1.4. (b) Model resulting from the inversion of binned data derived from that shown in (a), plotted without vertical exaggeration. Other parameters as in Fig. 7. The whole structure is substantially more conductive than that in Fig. 7(b), and the variation along the axis is less marked. This indicates that the true resistivity structure is 3-D in nature.

phase. In contrast, segment V8 to the north of this is underlain by a much narrower melt lens (1 km) of much more moderate reflection coefficient. Beneath segment V6 the magma chamber is of variable width and offset relative to the ridge axis and again displays a more moderate reflection coefficient than segment V7. The variable nature of the magma chamber here reflects the complexity of the ridge system at this point, where the Southern and Central Valu Fa Ridges overlap.

The thickness of seismic layer 2A decreases from about 1.3 km at the northern end of tow 2 to 1 km at its intersection with tow 3 (Turner *et al.* 1999). The base of layer 2A is often equated with the transition between porous and fractured extrusives (pillows and lava flows) and sheeted dykes. Since the extrusives would in general have a lower bulk resistivity than the sheeted dykes beneath, a thinning in layer 2A to the south could cause an increase in resistivity as observed. However, since the variations in resistivity extend to a depth of about 3 km, the variation in thickness of the seismically defined layer 2A cannot be the only factor governing the variation in resistivity. The variation in resistivity structure along-axis shown in Figs 7 and 8 follows the general trend of the segmentation, with the most rapid variations in structure occurring at or close to the segment boundaries. This suggests that at least part of the along-axis variation in resistivity structure is controlled by the magmatic segmentation of the ridge, and may be related to the current magma or heat budget within each segment. For example, the increase in resistivity with distance from the axis is much smaller beneath segment V7, which is currently underlain by a robust magma chamber, than under segment V6. The more rapid increase in resistivity off-axis beneath segment V6 may reflect the lower heat budget that this segment of the ridge is experiencing at present.

Across-axis structure

The presence of substantial variations in structure along the axis of the ridge presents problems for the 2-D interpretation of the bulk of the data set to give a vertical resistivity section perpendicular to the ridge. It is clear that any such 2-D interpretation, for which the direction in which the structure is invariant is parallel to the ridge axis, can only be approximate. To minimize the 3-D effects in the data, only signals recorded

during the along-axis tows when the source was between *LEMUR11*, *Ulysses* and *Lolita* in the north, and tow 3 in the south, were included. This corresponds to data collected within a single magmatic segment (segment V7) of the ridge. Data were partitioned into 500 m wide range bins and the mean amplitude and error in the mean calculated for each, in order to reduce the data volume. The binned data are shown in Fig. 9(a).

These data were inverted for a 2-D model of resistivity variations in a vertical plane perpendicular to the ridge axis. The resistivity structure is invariant parallel to the ridge axis and hence parallel to the along-axis tow tracks, so the effect of towing the source along these tracks can be modelled by assuming a stationary source, and considering a line of receivers parallel to the ridge axis, such that the source–receiver geometry at each offset is maintained. This reduces the number of source locations needed to describe the experiment to three (and hence reduces substantially the memory requirements). The requirement that there be three finite elements per skin depth meant that it was computationally prohibitive to include the 8 Hz data from tow 3 explicitly in the inversion. Instead, the results

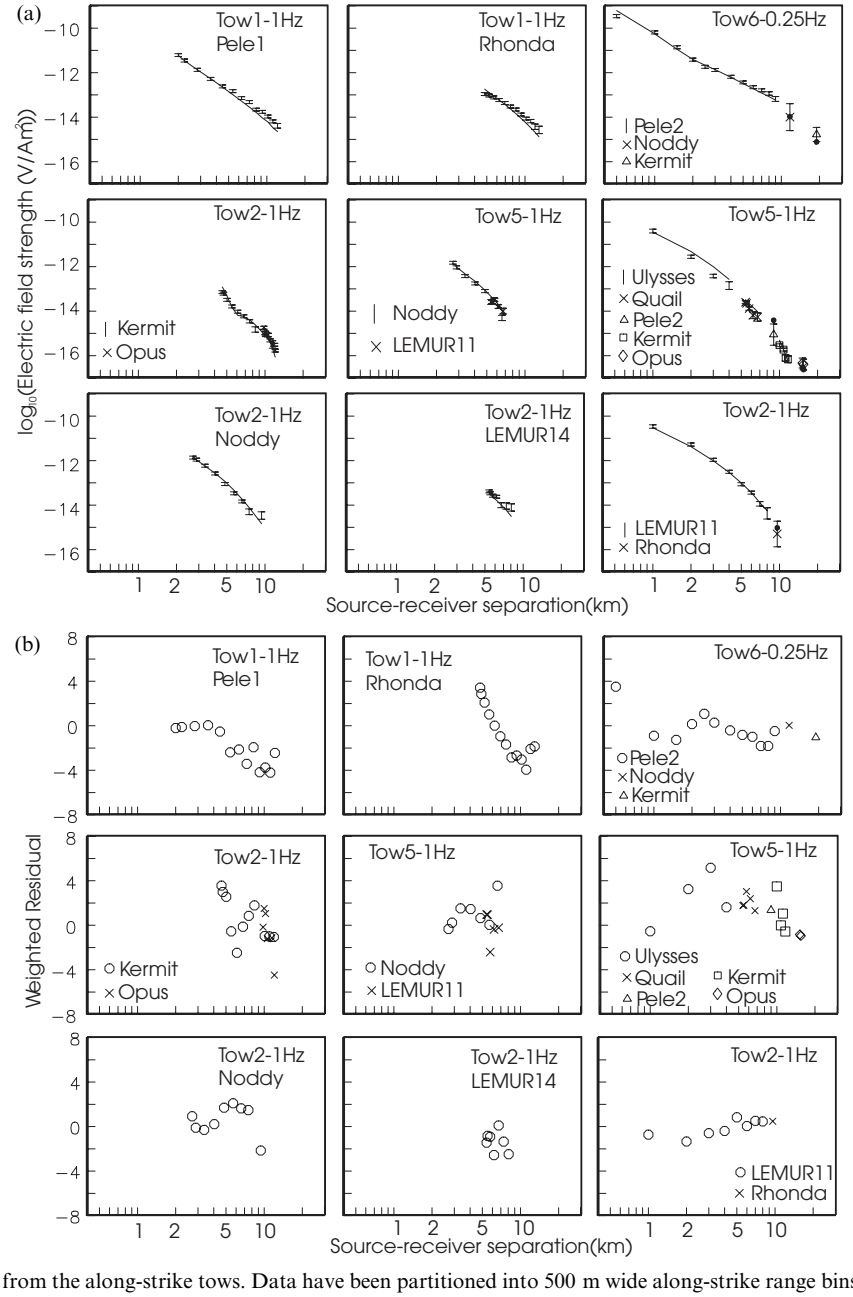

Figure 9. (a) Binned data from the along-strike tows. Data have been partitioned into 500 m wide along-strike range bins and the mean and error in the mean calculated in each. To minimize the effect of along-axis variations in structure, only signals recorded within one magmatic segment of the ridge (segment V7) are included. The solid lines/symbols show the response of the model resulting from inversion of this data set for a 2-D resistivity structure invariant parallel to the strike of the ridge (Fig. 10). The response fits the data to an RMS misfit level of 1.9. (b) Residuals between the data and response shown in (a). There is some bias remaining in the residuals after the inversion, especially in the data from *Pele1* and *Rhonda* collected during tow 1. However, reducing the misfit further does not significantly improve this bias, suggesting that remaining misfit is the result of 3-D effects in the data which cannot be explained with a 2-D structure.

from 1-D inversion of the 8 and 24 Hz data from tow 3 (Fig. 6) were interpolated across strike to produce a pseudo-2-D model of the upper 800 m of the crust. The 2-D inversion was then prejudiced to tend to this model in the upper 800 m of the structure. The result is a vertical section through the ridge which satisfies the 1 and 0.25 Hz data from the along-axis tow lines, whilst still being compatible with the 8 and 24 Hz data from the across-axis tow 3. For simplicity, the seafloor was modelled as flat. It will be shown later that the effect of including the real seafloor topography is negligible.

The final model, which fits the data to an RMS misfit level of 1.9, is shown in Fig. 10. The misfit level was chosen on the basis of structure in the residuals and the smoothness of the model. Although Fig. 9 shows that there is still significant structure in the residuals at this misfit level, reducing the required misfit further did not significantly improve the bias, whereas the roughness of the model increased rapidly. The bias in residuals is most significant for the 1 Hz data from tow 1. The data from *Rhonda* and *Pele1* at ranges greater than 3 km are systematically misfit by the 2-D model. This misfit is likely to be caused by 3-D effects in the data which cannot be accounted for with the current 2-D structure approximation. The 0.25 Hz data from tow 6 can be adequately explained by the 2-D model, suggesting that the 3-D structure is relatively small spatially (so that it affects the 1 Hz data without significantly perturbing the 0.25 Hz data). One possible origin for the three-dimensionality is conductive structure associated with the chain of off-axis seamounts trending approximately north-northwest, which intersects the northern part of tow 1. It is likely that the effect of the 3-D structure is manifest in the final model as the small, shallow region of low resistivity beneath instrument *Pele2*.

The remaining residuals display a satisfyingly random distribution and the agreement between instruments is good, even when the instruments are far apart (for example, the data from *Rhonda* collected during tow 2 is in excellent agreement with the data from *LEMUR11* collected during the same tow). This indicates that the instruments are correctly calibrated, both within and between instrument types. It also suggests that, leaving aside the problems with the data from tow 1 that are associated with off-axis anomalies, the structure within volcanic segment V7 of the ridge, from which the data subset was taken, is predominantly 2-D.

The ridge axis is characterized by a zone of low resistivity. Resistivity increases with distance from the axis; however, the increase occurs primarily in layers 2B/C and 3. The 1-D inversion of the higher-frequency data showed that layer 2A is extremely uniform across-axis and this result is born out by the 2-D inversion. The lack of vertical resistivity gradient at the axis is particularly noticeable and is in marked contrast to the resistivity structure observed at other mid-ocean ridge crests, where the resistivity rises sharply with depth below the seafloor, reaching 50–100 Ω m by a depth of 1–2 km. At the Valu Fa ridge, the resistivity is less than 10 Ω m at a depth of around 3 km. The implications of this will be discussed later.

Model sensitivity and resolution

Before any conclusions can be drawn from the structure shown in Fig. 10, it is essential to examine which features of the model are well constrained by the data. One approach is to perform a linearized sensitivity analysis around the final model, calculating the derivative of the response with respect to small changes in the model parameters. Fig. 11 shows the modulus of the sensitivity, S_j, calculated in this way, defined as

$$S_j = \frac{1}{A_j} \sum_i |J_{ij}| \tag{1}$$

and

$$J_{ij} = \frac{\partial d_i}{\partial m_j}, \tag{2}$$

where J_{ij} is the sensitivity of the ith datum, d_i, to small changes in the jth model parameter, m_j. In this case the data consist of $\log_{10}$ (electric field) and the model parameters are $\log_{10}$ (conductivity) within each region in the parametrization. The sensitivity is normalized by the area of each region, A_j, to remove its dependence on model parametrization. The data are sensitive to the upper 5 km of the structure, with the maximum sensitivity in the upper 3 km of the structure, between −12 km and 12 km across strike, corresponding to seismically defined layer 2 of the crust. There is a pronounced gap in sensitivity between instruments *Rhonda* and *LEMUR14*. Both of these instruments ceased recording shortly before tow 5, resulting in a lack of data coverage between them.

Although this type of sensitivity analysis is useful, it is only valid for small changes in the assumed final model. It therefore provides little information on which features of the structure are required by the data. Although a change in part of he model for which the sensitivity is high will result in a large change in the observed response, it is usually possible to compensate for this by changing another part of the model to produce a different, although equally valid, result. It is therefore instructive to use a combination of forward modelling and constrained inversion to target features of interest in the model and to see how well their properties may be bounded using the data set available.

Of particular interest is the low resistivity zone associated with the axis. The sensitivity analysis (Fig. 11) suggests that we can be confident about the structure within layer 2; however, it is not clear whether the low resistivities in layer 3 at the axis are required by the data, or are merely the result of vertical smearing of the low-resistivity zone in layer 2 caused by the regularization constraint in the inversion. To address this, the inversion was rerun, again to a required misfit level of RMS 1.9, this time allowing a break in the vertical smoothness at the layer 2/3 boundary (3.2 km below the seafloor). The resulting resistivity distribution in layer 2 was very similar to that shown in Fig. 10, although overall the resistivity of layer 2 was lower by up to 50 per cent. Layer 3 was almost uniform, with a resistivity of 60–80 Ω m, and there was no significant low-resistivity zone associated with the axis. This suggests that the structure in layer 2, and in particular the abnormally low vertical resistivity gradient, is well constrained and that the structure is at least as conductive as shown in Fig. 10.

The constraint on the structure in layer 3 is minimal and the low resistivity in layer 3 at the axis seen in Fig. 10 is not required by the data. This result is disappointing, especially since there is a large seismic velocity anomaly in layer 3 at the axis. Features smaller than a quarter of an electromagnetic skin depth cannot, in general, be resolved by CSEM data. If the resistivity of pure melt is taken to be 1 Ω m (e.g. Waff & Weill 1975), then the skin depth at 1 Hz is approximately 500 m. The

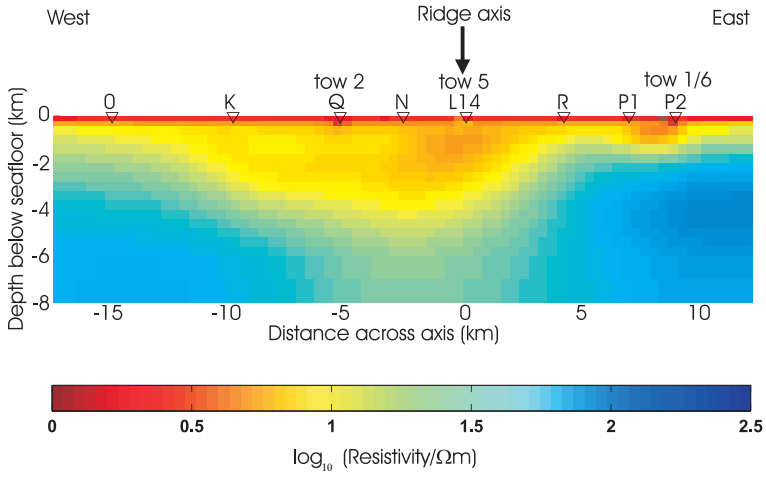

Figure 10. The result of inverting the 1 Hz and 0.25 Hz data from tows 1, 2, 5 and 6, shown in Fig. 9, plotted with no vertical exaggeration. The model is invariant perpendicular to the plane of the page (parallel to the ridge axis), and is overlain by a uniform layer of resistivity 0.3 Ω m representing the ocean. Labelled triangles mark the positions of the tow lines (which ran along the ridge axis) and receivers. The inversion started from a 400 m layer of resistivity 2 Ω m, overlying a uniform 10 Ω m half-space. The top 800 m of the model were prejudiced to converge to a pseudo-2-D model derived from inversion of the 8 and 24 Hz data from the across-axis tow line, which are sensitive to the shallow structure local to each receiver. This ensured the stability of the forward solution without having to fix any parameters, and also produced a model which satisfies the 1 and 0.25 Hz data whilst still being consistent with the higher-frequency data. The inversion reached the required misfit of RMS 1.9 in 2 iterations, and converged in a further 16 iterations.

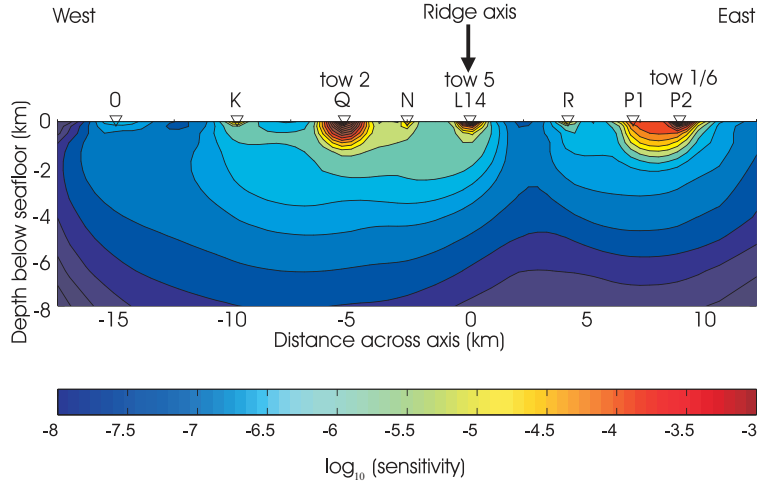

Figure 11. Magnitude of the survey sensitivity, as defined in eq. (1) for the model shown in Fig. 10. The data are sensitive to the upper 5 km of the structure, with the maximum sensitivity confined to the upper 3 km (seismically defined layer 2). See text for discussion.

melt lens imaged in the seismic reflection study (Collier & Sinha 1992a,b) has a thickness less than about 50 m and we would therefore not expect to resolve it using the CSEM data. The surrounding low-velocity zone, detected by the coincident wide-angle seismic data (Turner *et al.* 1999) is approximately 3 km thick and 4 km wide, and therefore under normal circumstances should be within the resolution of the CSEM data if it contained a large fraction of connected melt. MacGregor *et al.* (1998) used similar CSEM data to detect and quantify a zone of partial melt in the crust beneath the Reykjanes Ridge. However, as mentioned earlier, the resistivity of layer 2 at the Reykjanes Ridge was much greater than at the VFR, and the magma body was about 1 km shallower. The low layer 2 resistivity at the VFR has two consequences for the detection of deeper structure. First, the melt fraction in the mush zone surrounding the melt lens at the VFR is thought to be low ($\sim$1 per cent) on the basis of the seismic data (Turner *et al.* 1999). The contrast between it and the conductive layer 2 structure above may therefore be small. Second, the low layer 2 resistivity makes the entire ridge very attenuative to electromagnetic energy, which limits the penetration of signals into layer 3. Forward modelling suggests that even if the mush zone contained a very large fraction of melt, it would be hardly detectable because of the extreme attenuation of electromagnetic signals in layer 2.

A very noticeable feature of the structure shown in Fig. 10 is its asymmetry about the ridge axis. The degree to which this asymmetry is a required feature of the model was examined by reflecting the structure about the axis from east to west, and then from west to east, to form two new symmetric models. The responses of these models fit the data to RMS 4.5 and 4.6 respectively. The increase in misfit is largely due to the

under-fitting of data from instruments placed more than 5 km from the axis (*Rhonda* and *Pele* to the east of the axis and *Opus, Kermit* and *Quail* to the west). The lack of asymmetry closer to the axis could be due to the data gap and consequent lack of sensitivity between *LEMUR14* and *Rhonda*. However, beyond 5 km from the axis the structure is constrained, showing that resistivities east of the axis are higher than at equivalent distances west of the axis. Some degree of asymmetry would be expected because the active Tofua Island arc, located about 40 km west of the Valu Fa Ridge, is likely to influence the western part of the ridge to a greater extent than the eastern part, although the mechanism causing the elevated resistivity to the east of the axis is as yet unknown.

Effect of seafloor topography

A bathymetric profile across the Valu Fa Ridge parallel to tow 3 is shown in the upper panel of Fig. 13, plotted with no vertical exaggeration. The shallowest point is 2070 m below sea level, with a variation of about 750 m in seafloor depth along the profile. The effect of the seafloor topography was examined by distorting a rectilinear finite element mesh to follow the real seafloor, as described by MacGregor *et al.* (1998). Previous results (MacGregor *et al.* 1998) show that the character of the response is dominated by the subseafloor resistivity structure and that seafloor topography has a second-order effect on the response. Model parametrizations including seafloor topography are computationally expensive and the requirement in the current implementation of the forward modelling code that the source is placed at $z = 0$ means that a different mesh is required for each source location to be modelled. For these reasons the topography was not included in any of the inversions, but was added during the final stages of modelling to validate the conclusions.

To test the effect of the seafloor topography on the inversion result, synthetic data were generated from a simple 1-D layered structure consisting of a 500 m thick, 2 Ω m layer over a 1500 m thick, 10 Ω m layer, both overlying a 100 Ω m half-space (Fig. 12), which was deformed to follow the real seafloor topography. Synthetic data at 0.25 and 1 Hz were generated to mimic the real data set, with errors appropriate to the actual error distribution. These synthetic data were then inverted first using the conventional 1-D Occam algorithm of Constable *et al.* (1987), and second using the 2-D inversion. Fig. 12 shows the vertical resistivity structure from the 1-D inversion and vertical resistivity profiles through the 2-D inversion result taken at 2 km intervals between −14 km and 10 km across-axis. Both inversion methods recover a smoothed version of the initial model, as expected. The 1-D inversion result is almost identical to that obtained from inversion of synthetic data from a 1-D model without the seafloor topography included. The variation in resistivity across the 2-D model is small (much smaller than the variation seen in the model resulting from inversion of the real data). The model recovered by the 2-D inversion is in effect a 1-D layered structure, demonstrating that the effect of the seafloor topography does not map into spurious subseafloor structure if the data are inverted assuming that the seafloor is flat.

Including the realistic seafloor topography increases the misfit of the final model shown in Fig. 10 from 1.9 to 1.95. The change in the magnitude of the response is less than 1 per cent over the majority of the data set, with a maximum shift of just 2.5 per cent. Given this, and the inversion test described in the preceding paragraph, it is unlikely that inclusion of the seafloor topography in the inversion would have a significant effect on the result.

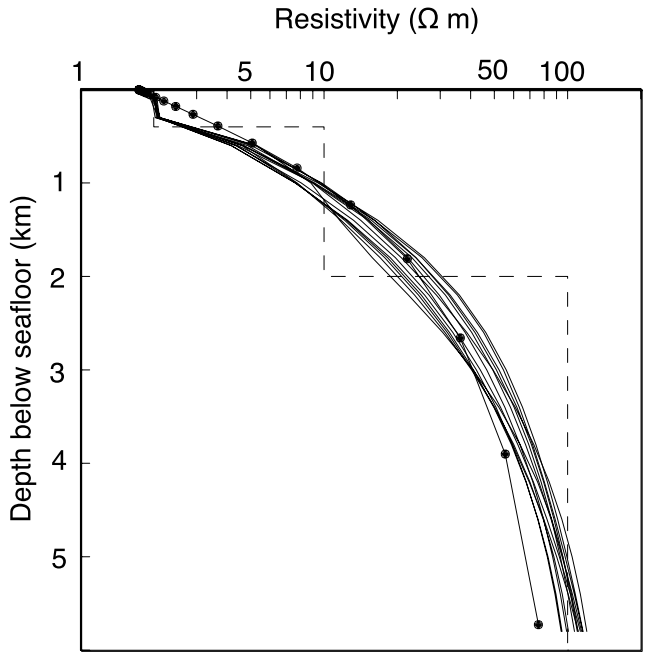

Figure 12. The effect of seafloor topography on inversion assuming a flat seafloor. The dashed line shows the initial 1-D model, which is overlain by a 0.3 Ω m half-space representing the ocean. This model was deformed to follow the realistic seafloor topography of the VFR, and then synthetic data generated to mimic the data collected during the CSEM experiment. These data were inverted assuming a flat seafloor using the 2.5-D inversion (solid lines) and a conventional 1-D Occam inversion (Constable *et al.* 1987) (filled circles). In both cases a smoothed version of the initial model is recovered. The small differences between the two inversion approaches are caused by differences in model parametrization. The solid lines are vertical resistivity profiles through the 2.5-D inversion result taken every 2 km between −14 km and 10 km across-axis. The model recovered by the 2.5-D inversion is essentially a horizontally layered structure, demonstrating that the effects of the seafloor topography do not map into spurious subseafloor structure if a flat seafloor is assumed.

DISCUSSION

The final 2-D resistivity structure shown in Fig. 10 shows that the axis of the Valu Fa Ridge is characterized by a region of low electrical resistivity in layer 2 of the crust. This variation is highlighted by plotting the resistivity anomaly (Fig. 12), defined as

$$\begin{aligned}\text{Anomaly} &= \log_{10}(\text{resistivity}) \\ &\quad - \log_{10}(\text{1d average resistivity at equivalent depth}) \\ &= \log_{10}\left(\frac{\text{2d resistivity}}{\text{1d average resistivity}}\right). \qquad (3)\end{aligned}$$

Fig. 13 shows a broad lower resistivity anomaly at the axis, extending up to 10 km from the ridge axis itself. The anomaly is primarily in layer 2 of the crust, the part of the structure to which the CSEM data are most sensitive.

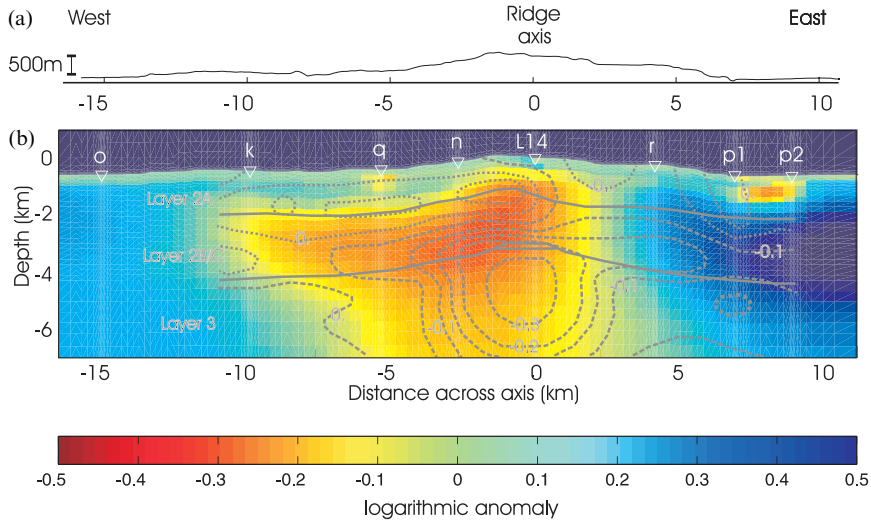

Figure 13. (a) Cross section of the VFR along tow 3 showing the seafloor topography. Data are taken from the swath bathymetry survey performed during the experiment, and are plotted without vertical exaggeration. The shallowest point at the ridge axis is a depth of 2070 m below sea level. The inclusion of this topography in the model shown in Fig. 10 has a negligible effect on the calculated response. (b) The resistivity anomaly at the Valu Fa Ridge, calculated relative to an average 1-D resistivity structure (see text for details). The anomaly plotted is the difference in $\log_{10}$ (Resistivity) between the 1-D average and 2-D inversion result, so that a negative value corresponds to a low-resistivity anomaly. Overlain on the resistivity anomaly is the seismic velocity anomaly (grey lines) calculated by Turner *et al.* (1999) from the wide-angle data collected along the seismic line coincident with tow 3. The magnitude of the anomaly is given in km/s relative to the average off-axis crustal resistivity profile.

The results of the CSEM survey can be compared with the results of the coincident wide-angle seismic experiment, presented by Turner *et al.* (1999), and the reflection seismic results of Collier & Sinha (1992a,b). The seismic structure at this location on the VFR is similar to that seen at other mid-ocean ridges, and can be divided into oceanic layers 2A, 2B/C and 3 according to the classification of Houtz & Ewing (1976), although seismic layer 2 is significantly thicker and crustal velocities are slightly lower than observed elsewhere. These differences can be attributed to the proximity of the ridge to the Tofua Island Arc and the andesitic composition of the magma produced. Overlain on the resistivity anomaly shown in Fig. 13 is the velocity anomaly calculated relative to the average off-axis vertical velocity profile, taken from Turner *et al.* (1999). The most prominent feature in the seismic model is the melt lens at a depth of 3 km below the seafloor at the ridge axis, surrounded by a zone of depressed seismic velocity in layer 3, interpreted as a mush zone containing a low fraction of partial melt. This mush zone, as delineated by the -0.2 km s^{-1} velocity anomaly contour, is approximately 4 km wide, and extends to within 2 km of the Moho, which lies at about 8.5 km below the seafloor.

The resistivity anomaly in layer 2A is small, in agreement with the results of the 1-D inversion of the 8 and 24 Hz data from tow 3. In contrast to the seismic anomaly, the most prominent resistivity anomaly is seen in seismic layer 2B/C, above the magma chamber in a region where the seismic velocity anomaly is small. Direct comparison of the resistivity structure with the velocity structure shows that whilst the seismic velocity shows a steep increase with depth as is usually seen in the upper crust, the coincident resistivity gradient is remarkably low. This suggests that the factors controlling the electrical resistivity and seismic velocity in layer 2 at the Valu Fa Ridge are markedly different.

The resistivity of solid volcanic rock is extremely high, so the bulk resistivity measured in a CSEM experiment is primarily controlled by the presence of more conductive phases. In the upper crust at a mid-ocean ridge which is a site of known hydrothermal activity, two such phases can be envisaged: salt water and hydrothermal mineralization. The presence of seawater-filled cracks has a profound effect on the measured resistivity (Drury & Hyndman 1979). Because the resistivity of salt water is several orders of magnitude less than that of the host rock, the bulk resistivity of the upper crust measured in a CSEM survey depends strongly on the resistivity of the permeating seawater, which itself varies with the temperature and ionic content (Nesbitt 1993). At 2 °C (ambient ocean floor temperature) the resistivity of sea water is 0.3 Ω m. At higher temperatures the resistivity falls, reaching a minimum of 0.04 Ω m at 350 °C then rising slightly. For temperatures below 350 °C, the resistivity of seawater, ρ_{SW}, at a temperature T is given to a good approximation by (e.g. Becker 1985)

$$\rho_{SW} = \left(3 + \frac{T\,(^{\circ}\mathrm{C})}{10}\right)^{-1}. \tag{4}$$

The conductivity of seawater increases almost linearly with salinity (Cox *et al.* 1967). Increasing the salinity of the fluid from 3 wt per cent (average ocean water salinity) to 10 wt per cent decreases the resistivity from 0.3 Ω m to about 0.08 Ω m at 2 °C (Nesbitt 1993). The presence of alteration products and hydrothermal mineralization within cracks can also affect the measured resistivity. The Valu Fa Ridge is a site of known active high- and low-temperature hydrothermal activity, and in many areas extensive iron-, copper- and zinc-rich sulphide mineralization has been observed (NAUTILAU group 1990; Fouquet *et al.* 1991a,b). Metal sulphides can have resistivities as low as 2×10^{-6} Ω m (Keller 1982) and seafloor resistivities as low as 0.1 Ω m have been observed in areas of massive sulphide mineralization on the Mid-Atlantic Ridge (Cairns *et al.* 1996) and Juan de Fuca Ridge (Nobes *et al.* 1992).

The simplest assumption, and a useful starting point, is that the crust is entirely suffused with seawater at ambient ocean floor temperatures. The overall bulk resistivity of a two-phase medium, consisting of a liquid (seawater in this case) and a solid of much higher resistivity, depends on the resistivity of each phase, the proportion of each present and their distribution. A medium with a high fluid content which is distributed in isolated pockets or pores will appear much more resistive than a medium in which the fluid content is much lower, but is distributed in a connected network throughout the solid. The Hashin–Shtrikman (HS) bounds describe an upper and lower limit on the conductivity (the inverse of resistivity) of an isotropic two-phase medium in which β is the volumetric fluid fraction (Schmeling 1986):

$$\mathrm{HS}^{-} = \sigma_s + \beta\left(\frac{1}{\sigma_l - \sigma_s} + \frac{1-\beta}{3\sigma_s}\right)^{-1}, \quad (5)$$

$$\mathrm{HS}^{+} = \sigma_l + (1-\beta)\left(\frac{1}{\sigma_s - \sigma_l} + \frac{\beta}{3\sigma_l}\right)^{-1}, \quad (6)$$

where σ_s is the conductivity of the solid and σ_l is the conductivity of the liquid. The upper HS bound, σ_{HS}, describes the conductivity of a medium in which the liquid forms a completely connected network. Assuming the upper HS bound in calculations therefore gives a good estimate of the volume of fluid which contributes to the conduction process, but may underestimate the total porosity if the medium contains isolated pores. The lower HS bound describes the situation in which the liquid phase is included in isolated pockets, and therefore does not contribute significantly to the overall resistivity of the medium.

The upper (connected) HS bound can be used to give a lower estimate on the crustal porosity. The resistivity of the solid rock is taken to be $10^4\ \Omega$ m, much higher than that of the fluid so that conduction within the host rock is negligible. Close to the seafloor, where the assumption that the fluid phase is seawater at ambient temperatures is most likely to be valid, this suggests porosities of approximately 21 per cent, consistent with estimates of porosity in layer 2A from the Mid Atlantic Ridge and East Pacific Rise based on electromagnetic (Evans *et al.* 1994; MacGregor *et al.* 1998) and seismic (Purdy 1987; Navin *et al.* 1998) data. Samples dredged from two sites on the VFR have vesicularities in the range 10–25 per cent by volume (Vallier *et al.* 1991), which could account for the porosity calculated from the resistivity providing that the vesicles are fully connected. High seafloor porosities are also consistent with the observation that the seafloor at the VFR is highly fractured and characterized by unconsolidated volcanic fragments.

At a depth of 2 km below the seafloor (about the centre of layer 2B/C), a porosity of 8 per cent is required to explain the resistivity at the axis if the crust is entirely saturated with cold seawater, falling to 2–3 per cent at 10 km from the axis. Such high porosities in layer 2B/C are inconsistent with drilling results from DSDP hole 504B in the Costa Rica Rift, which indicate porosities of less than 2 per cent in layer 2B/C (Becker 1985). In addition, a reduction of 5–6 per cent in porosity within 10 km of the axis would be expected to produce a seismic velocity anomaly in excess of 0.5 km s^{-1} (Greer 1999), much larger than the reduction of 0.1 km s^{-1} relative to the off-axis velocity actually observed in layer 2B/C (Turner *et al.* 1999). Increasing the temperature of the penetrating seawater to 10 °C reduces the required porosity to about 7 per cent on axis at a depth of 2 km below the seafloor, falling to 1–2 per cent in a distance of 10 km, but again this would produce a velocity anomaly larger than that observed. It is therefore unlikely that the low-resistivity anomaly at the axis is the result of large variations in the porosity of the crust.

Alternatively, instead of making an assumption about the temperature of the permeating fluid, which is unknown, it is reasonable to assume that the porosity depth profile does not change substantially with distance from the axis (on the scale of the CSEM experiment), since the velocity anomaly is less than 0.1 km s^{-1} in layer 2. Eqs (6) and (4) can then be combined to calculate the temperature necessary to explain a given resistivity. An example is shown in Fig. 14 for porosities between 1 and 5 per cent, again at a depth of 2 km below the seafloor. In all cases a broad high-temperature anomaly associated with the axis is predicted. If the porosity at 2 km depth below the seafloor at the axis were as high as 5 per cent, then the temperature need only be 25 °C to explain the observed resistivity. However, in this case the porosity would have to fall to at most 2 per cent to explain the off-axis resistivity. A reduction in porosity this large would produce a velocity anomaly of about 0.4 km s^{-1} at the axis (Greer 1999), which is not observed in the seismic data (Turner *et al.* 1999). Porosities of 2 per cent or less could explain the observed resistivity at all points across-axis, but this would require temperatures in excess of 100 °C extending at least 5 km from the axis itself. Although temperatures in excess of 200 °C in the dykes of layer 2B are predicted on the basis of alteration minerals in drilling and ophiolite studies (Alt 1995), it is not clear how far from the axis these temperatures persist. Theoretical models of fluid flow in high temperature hydrothermal systems suggest that the temperature falls off rapidly with distance from a region of active upflow, returning to close to ambient within a few hundred metres (Jupp & Schultz 2000). If this is the case, and the resistivity anomaly is not solely the result of the of the temperature of the permeating seawater, nor of large variations in porosity (since the seismic anomaly is small), then another mechanism must be found.

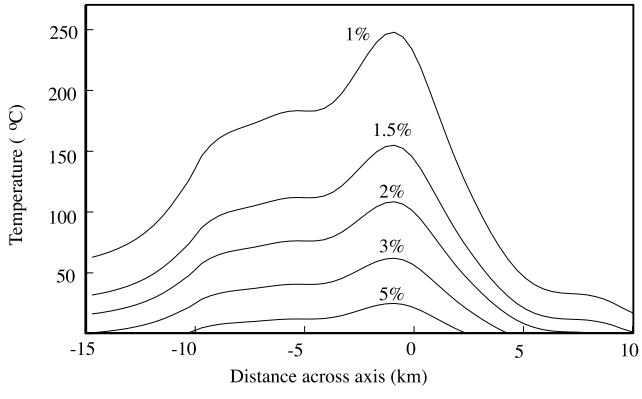

Figure 14. The temperature anomaly at the axis, assuming that the resistivity anomaly observed can be entirely explained by variations in temperature of the permeating seawater. Temperature at 2 km below the seafloor (about the centre of layer 2B/C) is plotted, as a function of distance across-axis from the location of *LEMUR14*. The upper (fully connected) Hashin–Shtrikman bound is assumed, and the variation of seawater resistivity with temperature is given by eq. (2). The ridge axis is characterized by a broad region of high temperature.

Two further possibilities can be envisaged. The first is that conductive hydrothermal deposits cause the low bulk resistivity observed. However, in order to produce an anomaly of the spatial scale observed, the mineralization would have to form a connected network throughout a region 3 km thick and over 5 km wide, extending up to 10 km along-axis. Massive sulphide deposits have been observed at the northern end of the CVFR and on the SVFR, but there is little evidence for massive sulphides along the rest of the CVFR (von Stackelberg 1990). Although large sulphide deposits thought to have been formed by mid-ocean ridge hydrothermal systems are observed on land, these usually have spatial scales on the order of a few hundred metres, rather than connected zones of mineralization on the scale of several kilometres (Franklin *et al.* 1981; Rhona 1988; Hannington *et al.* 1995). As well as massive sulphide deposits formed at the seafloor, the high permeability of the volcanics at the VFR could lead to extensive subsurface mineralization. However, such mineralization is likely to be confined to the zone where downward penetration of cold seawater meets the upward flow of heated hydrothermal fluids, probably around the base of layer 2A (von Stackelberg 1990; Alt 1995). Again this mechanism cannot account for low resistivities observed over such a large depth range. It is therefore likely that mineralization is a contributory rather than a governing factor.

The second possibility is that the fluids in the crust contain a higher concentration of salt than normal ocean water, thus decreasing the bulk resistivity of the crust without affecting the seismic velocity. Lecuyer *et al.* (1999) studied the composition of fluid inclusions in samples from three Valu Fa Ridge hydrothermal sites. They found high salinity liquids in some samples (up to 30 wt per cent NaCl), which they attributed to a combination of phase separation in the hydrothermal system—a consequence of the shallow setting of the Lau Basin hydrothermal fields—and production of high-salinity brines from water exsolved from the magma chamber, which in the back-arc setting contains silicic melt with a high water content. At 3 km below the seafloor, phase separation from the hydrous fluid exsolved from magma is likely to occur in narrow cracks, conditions that would favour the segregation of the vapour and liquid, resulting in dense briney fluid remaining at depth (Goldfarb & Delaney 1988; Lecuyer *et al.* 1999). The low-resistivity anomaly observed could be the result of brines produced either on axis during an earlier phase of volcanic and hydrothermal activity at this segment of the ridge, or more recently from the current stage of magma chamber recharge (Collier & Sinha 1992b).

The true cause of the low axial resistivity in layer 2 is likely to be a combination of porosity, temperature, salinity and mineralization effects, which cannot be distinguished on the basis of the electromagnetic data alone. In particular, in a two-phase medium there is a trade-off between the porosity of the medium and the conductivity of the permeating fluid phase, which is controlled primarily by temperature and salinity. Combining the electrical resistivity and seismic velocity using the effective medium approach of Greer (1999) can potentially remove some of the ambiguities inherent in either the electromagnetic or seismic technique alone. This will be the subject of future work. However, it is clear that the seismic and electromagnetic data are sensing very different properties of the crust. The seismic velocity structure (Turner *et al.* 1999) shows that there is a steep velocity gradient in layer 2, with a high-velocity lid above the magma chamber. In contrast, the vertical resistivity gradient at the axis is remarkably small. Because the low electrical resistivity detected at the axis extends from the seafloor to a depth of at least 3 km (the depth of the seismically imaged magma chamber), it is likely that whatever hot and/or briney hydrothermal fluids are present at this point on the Valu Fa Ridge extend in a connected network of fractures or pores to or very close to the magma chamber itself.

CONCLUSIONS

Controlled-source electromagnetic sounding provides a means of determining crustal-scale electrical resistivity structure, which can provide valuable constraints on the physical properties of the crust. This paper describes a survey carried out on the southern portion of the Central Valu Fa Ridge in the Lau Basin. Although the structure of layer 3 of the crust cannot be determined using this data set, layer 2 is well constrained and its structure is very different from that seen at other mid-ocean ridge crests. The main conclusions are summarized below.

(i) Resistivity in layer 2A is remarkably uniform across-axis between 9 km to the east and 15 km to the west. The resistivity rises from 2 Ω m at the seafloor to around 8–10 Ω m at 800 m below the seafloor. Resistivities are consistent with about 20 per cent connected porosity, saturated with seawater at 2 °C.

(ii) In layer 2B/C, resistivity increases with distance from the axis; however, the vertical resistivity gradient is low, with resistivities only slightly greater than 10 Ω m at 3 km depth below the seafloor. This is in marked contrast to the results from other CSEM surveys at ridge crests, where the resistivity at equivalent depths can be up to an order of magnitude higher than at the Valu Fa Ridge (Evans *et al.* 1991, 1994; MacGregor *et al.* 1998).

(iii) The lack of vertical resistivity gradient in layer 2 also contrasts strongly with the results of the coincident seismic experiment, which found that the seismic velocity structure was similar to that observed at other mid-ocean ridges, with a steep velocity gradient through layer 2. This indicates that the electromagnetic and seismic data are sensitive to very different physical properties of the crust.

(iv) The low resistivity at the axis, coupled with the lack of a large seismic velocity anomaly in layer 2B/C at the axis, can be explained by the pervasive penetration of hot and/or briney fluids to or close to the magma chamber itself. Although a high-seismic-velocity lid is observed above the magma chamber, there is no corresponding high resistivity lid in layer 2. This observation could be explained by the presence of hot briney fluids produced by phase separation in the axial hydrothermal system or exsolved from the melt body, which would dramatically lower the electrical resistivity without altering the seismic velocity significantly.

ACKNOWLEDGMENTS

We would like to thank the officers and crew of the *RV Maurice Ewing*, Peter Carter, Michael MacCormack, Steven Riches, David Booth and members of the EW95/12 scientific party, without whom none of this would have been possible. We are also grateful to Prof. Adam Schultz for use of the high performance computing facility at the Institute of Theoretical

Geophysics, Cambridge. 1-D and 2.5-D forward modelling were carried out using the codes of A. D. Chave and M. J. Unsworth respectively. The paper was much improved by the comments of Graham Heinson and an anonymous reviewer. This research, including the involvement of the Scripps Institution of Oceanography seafloor receivers, was supported by the Natural Environment Research Council (Grant No. SGST/02/1123 and GR3/9414). LM was supported by a Fellowship from Downing College, Cambridge, and by a Leverhulme Trust Special Research Fellowship.

REFERENCES

Alt, J.C., 1995. Sub-seafloor processes in mid-ocean ridge hydrothermal systems, *Am. geophys. Un. Monogr.,* **91,** 85–114.

Becker, K., 1985. Large scale electrical resistivity and bulk porosity of the oceanic crust, deep sea drilling project hole 504B, Costa Rica rift, *Init. Rept. DSDP,* **83,** 419–427.

Cairns, G.W., Evans, R.L. & Edwards, R.N. 1996, A time domain electromagnetic survey of the TAG hydrothermal mound, *Geophys. Res. Lett.,* **23,** 3455–3458.

Chave, A.D. & Cox, C.S., 1982. Controlled electromagnetic sources for measuring electrical conductivity beneath the oceans—I, Forward Problem and model study, *J. geophys. Res.,* **87,** 5327–5338.

Collier, J.S. & Sinha, M.C., 1992a. Seismic mapping of a magma chamber beneath the Valu Fa Ridge, Lau Basin, *J. geophys. Res.,* **97,** 14 031–14 053.

Collier, J.S. & Sinha, M.C., 1992b. The Valu Fa Ridge: The pattern of volcanic activity at a back-arc spreading centre, *Mar. Geol.,* **104,** 243–263.

Constable, S.C. & Cox, C.S., 1996. Marine controlled-source electromagnetic sounding—II: The PEGASUS experiment, *J. geophys. Res.,* **101,** 5519–5530.

Constable, S.C, Parker, R.L. & Constable, C.G., 1987. Occam's inversion: A practical algorithm for generating smooth models from electromagnetic data, *Geophysics,* **52,** 289–300.

Cox, R.A., Culkin, F. & Riley, J.P., 1967. The electrical conductivity/chlorinity relationship in natural seawater, *Deep Sea Res.,* **14,** 203–220.

de Groot-Hedlin, C. & Constable, S., 1990. Occam's inversion to generate smooth, 2-dimensional models from magnetotelluric data, *Geophysics,* **55,** 1613–1624.

Drury, M.J. & Hyndman, R.D., 1979. The electrical resistivity of oceanic basalts, *J. geophys. Res.,* **84,** 4537–4545.

Evans, R.L., Constable, S.C., Sinha, M.C., Cox, C.S. & Unsworth, M.J., 1991. Upper crustal structure of the East Pacific Rise near 13°N, *Geophys. Res. Lett.,* **18,** 1917–1920.

Evans, R.L., Sinha, M.C., Constable, S.C. & Unsworth, M.J., 1994. On the electrical nature of the axial melt zone at 13°N on the East Pacific Rise, *J. geophys. Res.,* **99,** 577–588.

Evans, R.L., *et al.*, 1999. Asymmetric electrical structure in the mantle beneath the East Pacific Rise at 17°S, *Science,* **286,** 752–755.

Flosadóttir, A.H. & Constable, S.C., 1996. Marine controlled-source electromagnetic sounding—I: Modelling and experimental design, *J. geophys. Res.,* **101,** 5507–5517.

Flosadóttir, A.H. & MacGregor, L.M., 1999. Induction sources in the ocean: A model code for oceanic and controlled-sources, *EOS, Trans. Am. geophys. Un.,* **80,** 293.

Forsyth, D.W. *et al.*, 1998. Imaging the deep seismic structure beneath a mid-ocean ridge: the MELT experiment, *Science,* **280,** 1215–1218.

Fouquet, Y. *et al.*, 1991a. Hydrothermal activity and metallogenesis in the Lauback-arc basin, *Nature,* **349,** 778–781.

Fouquet, Y. *et al.*, 1991b. Hydrothermal activity in the Lau back-arc basin: sulphides and water chemistry, *Geology,* **19,** 303–306.

Franklin, J.M., Lydon, J.W. & Sangster, D.F., 1981. Volcanic associated massive sulphide deposits, *Econ. Geol. 75th Anniv. Vol,* 485–627.

Goldfarb, M. & Delaney, J.R., 1988. Response of two phase fluids to fracture configurations within submarine hydrothermal systems, *J. geophys. Res.,* **93,** 4585–4594.

Greer, A.A., 1999. Use of effective medium techniques to integrate seismic and controlled-source electromagnetic data, *LITHOS Sci. rept,* **1,** 111–114.

Hannington, M.D., Jonasson, I.R., Herzig, P.M. & Petersen, S., 1995. Physical and chemical processes of seafloor mineralization at mid-ocean ridges, *Am. geophys. Un. Monogr.,* **91,** 115–157.

Herzig, P.M., von Stackelberg, U. & Petersen, S., 1990. Hydrothermal mineralization from the Valu Fa Ridge, Lau Basin, *Mar. Min.,* **9,** 271–301.

Houtz, R. & Ewing, J., 1976. Upper crustal structure as a function of plate age, *J. geophys. Res.,* **81,** 4143–4161.

Jenner, G.A., Cawood, P.A., Rautenschlein, M. & White, W.M., 1987. Composition of back-arc volcanics, Valu Fa Ridge, Lau Basin: Evidence for a slab derived component in their mantle source, *J. Volc. Geotherm. Res.,* **32,** 209–222.

Jupp, T. & Schultz, A., 2000. A thermodynamic explanation for black smoker temperatures, *Nature,* **403,** 880–883.

Keller, G.V., 1982. Electrical properties of rocks and minerals, in *Handbook of Physical Properties of Rocks,* Vol. 1, pp. 217–293, ed. Carmichael, R.S., CRC Press, Boca Raton, FL.

Lecuyer, C., Dubois, M., Marignac, C., Gruau, G., Fouquet, Y. & Ramboz, C., 1999. Phase separation and fluid mixing in subseafloor back arc hydrothermal systems: A microthermometric and oxygen isotope study of fluid inclusions in the barite-sulphide chimneys of the Lau Basin, *J. geophys. Res.,* **104,** 17 911–17 927.

MacGregor, L.M., 1999. Marine controlled source electromagnetic sounding: Development of a regularised inversion for 2-dimensional resistivity structures, *LITHOS Sci. Rrpt,* **1,** 103–109.

MacGregor, L.M. & Sinha, M.C., 2000. Use of marine controlled-source electromagnetic sounding for subbasalt exploration, *Geophys. Prospect.,* **48,** 1091–1106.

MacGregor, L.M., Constable, S.C., Sinha, M.C., 1998. The RAMESSES experiment—III. Controlled-source electromagnetic sounding of the Reykjanes Ridge at 57°45′N, *Geophys. J. Int.,* **135,** 772–789.

McGillivray, P.R., Oldenburg, D.W., Ellis, R.G. & Habashy, T.M., 1994. Calculation of sensitivities for the frequency-domain electromagnetic problem, *Geophys. J. Int.,* **116,** 1–4.

Morton, J.L. & Sleep, N.H., 1985. Seismic reflections from a Lau Basin magma chamber, in *Geology and Offshore Resources of Pacific Island Arcs—Tonga region,* pp. 441–453, eds Scholl, D.W. & Vallier, T.L., Circum-Pacific Council for Energy and Mineral Resources, Earth Sci. Ser. No. 2, Houston, TX.

NAUTILAU Group, 1990. Hydrothermal activity in the Lau Basin, *EOS, Trans. Am. geophys. Un.,* **71,** 678–679.

Navin, D.A., Peirce, C.P. & Sinha, M.C., 1998. RAMESSES II—Evidence for accumulated melt beneath a slow-spreading ridge from wide-angle refraction and multichannel reflection seismic profiles, *Geophys. J. Int.,* **135,** 746–772.

Nesbitt, B.E., 1993. Electrical resistivities of crustal fluids, *J. geophys. Res.,* **98,** 4301–4310.

Nobes, D.C., Law, L.K. & Edwards, R.N., 1992. Results of a sea-floor electromagnetic survey over a sedimented hydrothermal area on the Juan de Fuca Ridge, *Geophys. J. Int.,* **110,** 333–346.

Parson, L.M. *et al.*, 1990. Role of ridge jumps and ridge propagation in the tectonic evolution of the Lau back-arc basin, Southwest Pacific, *Geology,* **18,** 470–473.

Parson, L.M. *et al.*, 1993. En echelon axial volcanic ridges at the Reykjanes Ridge: A life cycles of volcanism and tectonics, *Earth planet. Sci. Lett.,* **117,** 73–87.

Purdy, G.M., 1987. New observations of the shallow seismic structure of young oceanic crust, *J. geophys. Res.,* **92,** 9351–9362.

Rona, P.A., 1988. Hydrothermal mineralisation at oceanic ridges, *Canadian Mineralogist,* **26,** 431–465.

Schmeling, H., 1986. Numerical models on the influence of partial melt on elastic, anelastic and electrical properties of rocks. Part II: electrical conductivity, *Phys. Earth planet. Inter.,* **43,** 123–136.

Sinha, M.C., Patel, P.D., Unsworth, M.J., Owen, T.R.E. & MacCormack, M.G.R., 1990. An active source electromagnetic sounding system for marine use, *Mar. Geophys. Res.,* **12,** 59–68.

Sinha, M.C., Constable, S.C., Peirce, C., White, A., Heinson, G., MacGregor, L.M. & Navin, D.A., 1998. Magmatic processes at slow spreading ridges: implications of the RAMESSES experiment at 57°45′N on the Mid Atlantic Ridge, *Geophys. J. Int.,* **135,** 731–745.

Smith, B.D. & Ward, S.H., 1974. Short note on the computation of polarisation ellipse parameters, *Geophysics,* **39,** 867–869.

Staudigel, H., Kastner, M. & Sturz, A., 1986. Delta ^{18}O and $^{87}Sr/^{86}Sr$ of calcites from the basaltic basement of DSDP hole 597: Timing and temperature of alteration, *Init. Rept. DSDP.,* **92,** 499–503.

Taylor, B., Zellmer, K., Martinez, F. & Goodliffe, A., 1996. Seafloor spreading in the Lau back-arc basin, *Earth planet. Sci. Lett.,* **144,** 35–40.

Turner, I.M., Peirce, C. & Sinha, M.C., 1999. Seismic imaging of the axial region of the Valu Fa Ridge, Lau Basin—the accretionary processes of an intermediate back-arc spreading ridge, *Geophys. J. Int.,* **138,** 495–519.

Unsworth, M.J., 1991. Electromagnetic exploration of the oceanic crust with controlled-sources, *PhD. thesis,* University of Cambridge, Cambridge.

Unsworth, M.J., 1994. Exploration of a mid-ocean ridge with a frequency-domain EM system, *Geophys. J. Int.,* **116,** 447–467.

Unsworth, M.J. & Oldenburg, D., 1995. Subspace inversion of electromagnetic data: application to mid-ocean ridge exploration, *Geophys. J. Int.,* **123,** 161–168.

Unsworth, M.J., Travis, B.J. & Chave, A.D., 1993. Electromagnetic induction by a finite electric dipole over a 2-D earth, *Geophysics,* **58,** 198–214.

Vallier, T.L. *et al.*, 1991. Sub-alkaline andesite from the Valu Fa Ridge, a back-arc spreading center in the Lau Basin: petrogenesis, comparative chemistry and tectonic implications, *Chem. Geol.,* **91,** 227–256.

von Stackelberg, U., 1990. R.V. Sonne cruise SO48: Summary of results testing a model of mineralisation, *Mar. Min.,* **9,** 135–144.

von Stackelberg, U. *et al.*, 1988. Active hydrothermalism in the Lau back-arc basin (SW Pacific): First results from the SONNE cruise 48, *Mar. Min.,* **7,** 431–442.

von Stackelberg, U. & Wiedicke, M., 1990. Interpretation of bottom photographs from active spreading ridges in the Lau Basin, *Mar. Min.,* **9,** 247–270.

Waff, H.S. & Weill, D.F., 1975. Electrical conductivity of magmatic liquids: effects of temperature, oxygen fugacity and composition, *Earth planet. Sci. Lett.,* **28,** 254–260.

Webb, S.C, Constable, S.C., Cox, C.S. & Deaton, T.K., 1985. A seafloor electric field instrument, *J. Geomag. Geoelectr.,* **37,** p1115–1129.

Webb, S. & Cox, C.S., 1982. Electromagnetic fields induced at the seafloor by Rayleigh-Stoneley waves, *J. geophys. Res.,* **87,** 4093–4102.

Webb, S. & Cox, C.S., 1986. Observations and modelling of seafloor microseisms, *J. geophys. Res.,* **91,** 7343–7358.

Wiedicke, M. & Collier, J., 1993. Morphology of the Valu Fa spreading ridge in the Southern Lau Basin, *J. geophys. Res.,* **98,** 11 769–11 782.

Wiedicke, M. & Kudrass, H.-R., 1990. Morphology and tectonic development of the Valu Fa Ridge, Lau Basin (Southwest Pacific): Results from a deep-towed side-scan sonar survey, *Mar. Min.,* **9,** 145–156.

Young, P.D. & Cox, C.S., 1981. Electromagnetic active source sounding near the East Pacific Rise, *Geophys. Res. Lett.,* **8,** 1043–1046.